Bioactive Materials 50 (2025) 152–170

Contents lists available at ScienceDirect

Bioactive Materials

journal homepage: www.keaipublishing.com/en/journals/bioactive-materials

Bidirectional modulation of glycolysis using a multifunctional nanocomposite hydrogel promotes bone fracture healing in type 2 diabetes mellitus

Shengming Zhang [a,b,1], Weixian Hu [a,b,1], Yanzhi Zhao [a,b,1], Yuheng Liao [a,b,1], Kangkang Zha [a,b], Wenqian Zhang [a,b], Chenyan Yu [a,b], Jiewen Liao [a,b], Hui Li [a,b], Wu Zhou [a,b,****], Faqi Cao [a,b,***], Bobin Mi [a,b,**], Guohui Liu [a,b,*]

[a] Department of Orthopaedics, Union Hospital, Tongji Medical College, Huazhong University of Science and Technology, Wuhan, 430022, China
[b] Hubei Province Key Laboratory of Oral and Maxillofacial Development and Regeneration, Wuhan, 430022, China

ARTICLE INFO

Keywords:
Fracture healing
Diabetes
Glycolysis
Hydrogel
Anti-inflammation

ABSTRACT

Fracture healing in patients with type 2 diabetes mellitus (T2D) is markedly impaired, characterized by a prolonged inflammation phase and defective osteoblast differentiation at the fracture site. In this study, we identified aberrant cellular glycolysis at T2D fracture sites, with bone marrow mesenchymal stem cells (BMSCs) exhibiting suppressed glycolysis and macrophages displaying enhanced glycolysis, mediated by the dysregulation of hypoxia-inducible factor-1α (HIF-1α). To rectify these metabolic imbalances, we developed a multifunctional nanocomposite PN@MHV hydrogel. Myricitrin, a flavonoid glycoside, forms the MHV hydrogel by cross-linking with HA-PBA and PVA via hydrogen bonds, and upregulates glycolysis through HIF-1α, thus promoting osteoblast differentiation under high glucose environment. To further regulate the inflammatory microenvironment, we incorporated nanoparticles loaded with PX-478, a HIF-1α specific inhibitor, into the hydrogel, with folic acid covalently modified to target proinflammatory M1 macrophages. This PN@MHV hydrogel bidirectionally regulated glycolysis via HIF-1α, enhancing osteoblast differentiation while attenuating macrophage-mediated inflammation. Comprehensive in vitro and in vivo experiments in a T2D fracture mouse model confirmed the hydrogel's ability to improve the inflammatory microenvironment and accelerate bone healing. Our findings underscore the therapeutic potential of targeting cellular glycolysis as a promising approach for enhancing fracture healing in diabetic patients.

1. Introduction

Diabetes mellitus is a well-established risk factor for fractures, with profound implications for bone healing [1]. It is a metabolic disorder that disrupts many critical events during the bone healing process, leading to delayed union or non-union of fractures in patients [2,3]. As the global prevalence of diabetes mellitus continues to rise, especially type 2 diabetes mellitus (T2D), the urgent need for effective interventions to prevent the occurrence of diabetic fracture complications has become paramount [4,5]. The diabetic bone microenvironment, characterized by hyperglycemia, excessive inflammation, and elevated reactive oxygen species (ROS), poses substantial challenges for conventional fracture healing strategies [3,6,7]. Therefore, elucidating the molecular mechanisms underlying these pathologies is critical for developing specific treatment strategies.

Within the bone healing microenvironment, a range of cellular

Peer review under the responsibility of editorial board of Bioactive Materials.

* Corresponding author. Hubei Province Key Laboratory of Oral and Maxillofacial Development and Regeneration, Wuhan, 430022, China.
** Corresponding authors. Hubei Province Key Laboratory of Oral and Maxillofacial Development and Regeneration, Wuhan, 430022, China.
*** Corresponding author. Hubei Province Key Laboratory of Oral and Maxillofacial Development and Regeneration, Wuhan, 430022, China.
**** Corresponding authors. Hubei Province Key Laboratory of Oral and Maxillofacial Development and Regeneration, Wuhan, 430022, China.
E-mail addresses: 2016XH0120@hust.edu.cn (W. Zhou), 13971293030@163.com (F. Cao), mibobin@hust.edu.cn (B. Mi), liuguohui@hust.edu.cn (G. Liu).
[1] These authors contributed equally to this study: Shengming Zhang, Weixian Hu, Yanzhi Zhao, Yuheng Liao.

https://doi.org/10.1016/j.bioactmat.2025.03.020
Received 7 November 2024; Received in revised form 25 March 2025; Accepted 26 March 2025

processes orchestrate the inflammatory and reparative phases of early regeneration. The timely transition of the inflammatory phase into repair phase is crucial to progression towards repair [8]. However, in diabetic patients, persistent hyperinflammation—manifested by a failed transition from proinflammatory M1 macrophages to anti-inflammatory M2 macrophages—prolongs the inflammatory phase, thereby hindering fracture healing [9–11]. Furthermore, osteoblasts, critical for bone regeneration, exhibit impaired osteoblast differentiation in diabetic fracture sites, exacerbating the healing delay [12–14]. Glucose metabolism is the main source of the cellular energy production. While mitochondrial oxidative phosphorylation serves as the main energy source for most mature cells, under hypoxic conditions, cytoplasmic glycolytic flux is increased to fulfill cellular ATP requirements [15]. Cells also exhibit high levels of glycolysis when oxygen is available, a phenomenon known as the aerobic glycolysis or the "Warburg effect" [16]. Initially identified in cancer cells, as research progressed it was found that this metabolic shift to high levels of glycolysis contributes to various biological processes, including rapid cell proliferation, differentiation, phenotype, and function [17–19]. Notably, aerobic glycolysis is upregulated during osteoblast differentiation and the activation of proinflammatory M1 macrophages [19–22]. Recent studies have revealed impaired osteoblast glycolysis in T2D mice, and the promotion of glycolysis has been shown to attenuate bone loss in diabetic models [12]. Conversely, the suppression of macrophage glycolysis exerts significant anti-inflammatory effects, highlighting the dual potential of glycolysis modulation in bone healing [23,24]. Despite this, current therapeutic strategies have largely focused on unidirectional regulation of glycolysis in single cell types, neglecting the complex changes of glycolysis and dynamic interplay across multiple cell populations within the diabetic microenvironment [12,25].

Hypoxia-inducible factor-1 (HIF-1), a key transcriptional activator, plays a central role in cellular adaptation to hypoxia by promoting the expression of a variety of cellular glycolytic enzymes through stabilization of its subunit HIF-1α [15,26]. Thus HIF-1α could serve as an important mediator molecule in the regulation of glycolysis. Hydrogels, renowned for their hydrophilicity, stability, drug encapsulation capabilities, and biocompatibility, are widely used in tissue engineering applications. Recent advances have demonstrated that phenylboronic acid-grafted hyaluronic acid (HA-PBA) confers glucose responsiveness to hydrogels, making them well-suited for high glucose environments in diabetic patients, enabling controlled, on-demand drug release [27].

In this study, we developed a hydrogel system targeting both bone marrow mesenchymal stem cells (BMSCs) and M1 macrophages to enable bidirectional regulation of glycolysis. We observed dysregulation of HIF-1α and the key glycolytic protein GLUT1 in fracture-localized BMSCs and M1 macrophages of diabetic mice, attributed to the

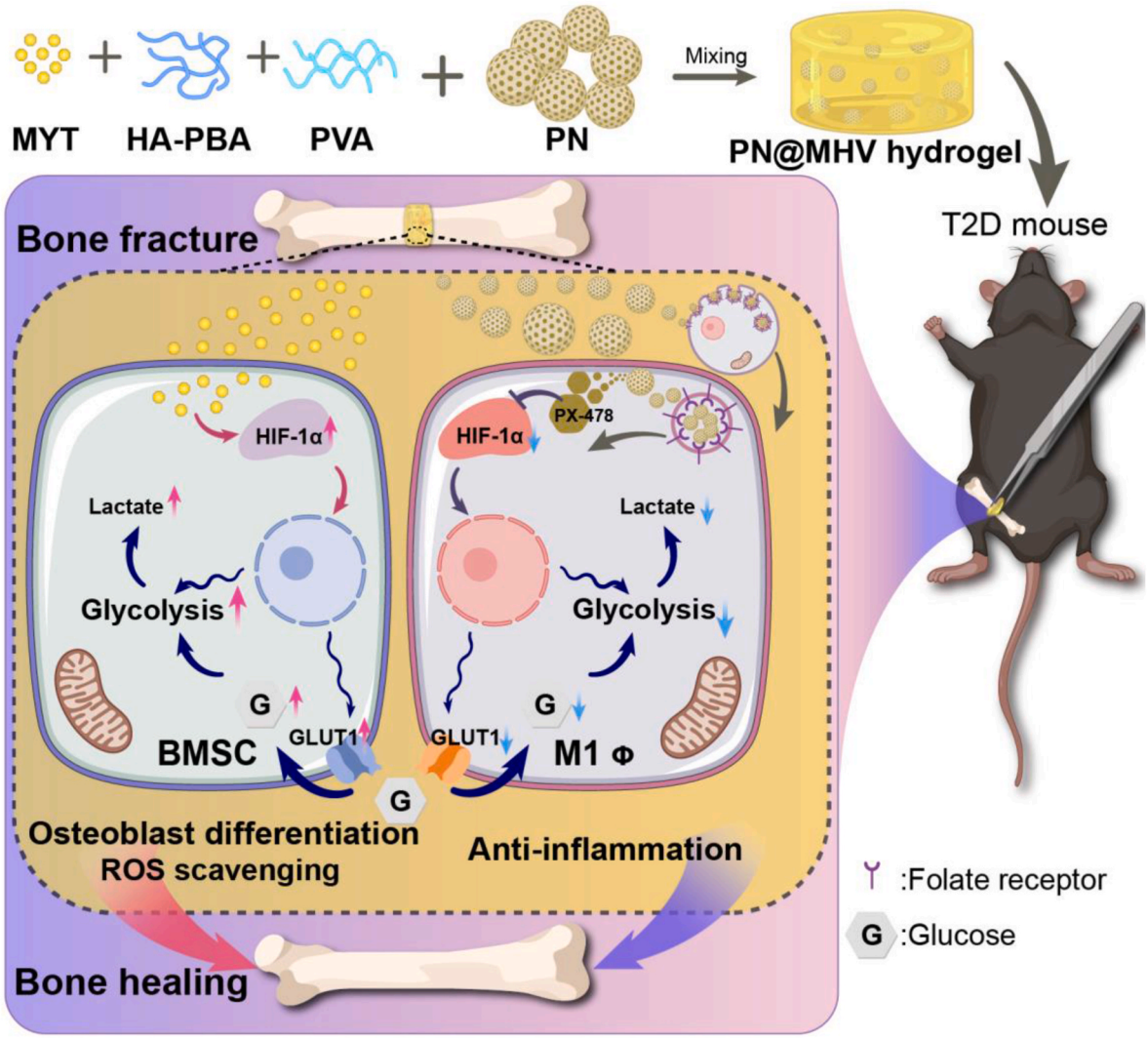

Fig. 1. Schematic illustration of the preparation of PN@MHV hydrogel and the bidirectional modulation of glycolysis in BMSCs and macrophages promoting T2D fracture healing.

hyperglycemic environment. Myricitrin (MYT) demonstrated a beneficial effect in upregulating HIF-1α expression and enhancing glycolysis under high glucose environment. Furthermore, MYT formed extensive hydrogen bonds with the hydrogel precursors HA-PBA and polyvinyl alcohol (PVA), enabling cross-linking to form the MYT-HA-PBA-PVA (MHV) hydrogel. To achieve bidirectional regulation of glycolysis, we incorporated liposomal nanoparticles loaded with the HIF-1α inhibitor PX-478, covalently modified with folic acid for M1 macrophage targeting, into the MHV (PN@MHV) hydrogel [28]. This hydrogel system simultaneously promoted osteoblast differentiation by enhancing glycolysis in BMSCs, while inhibiting glycolysis in M1 macrophages to mitigate the inflammatory microenvironment (Fig. 1). Additionally, in vivo studies demonstrated the efficacy of PN@MHV hydrogels in promoting fracture healing and reducing local inflammation in a T2D mouse model, presenting a novel therapeutic strategy for the treatment of fractures in diabetic patients.

2. Materials and methods

2.1. Materials

Hyaluronic acid (1.0 MDa), 4-(4,6-Dimethoxy1,3,5-triazin-2-yl)-4-methylmorpholinium chloride, 3-Aminomethylphenyl boronic acid hydrochloride, and MYT were purchased from Aladdin (Shanghai, China). PX-478 and folic acid were purchased from MCE (Shanghai, China). Lecithin and cholesterol were purchased from Sigma-Aldrich (USA).

2.2. Preparation and characterization of PN

15 mg of lecithin, 85 mg of cholesterol, and 10 mg of DSPE-PEG2000-folic acid were dissolved in chloroform of 4 ml volume, the organic reagents were removed by rotary evaporation to form thin films. The above films were hydrated with 250 nM ammonium sulphate solution. The generated solution was squashed through 400, 200 and 100 nm polycarbonate membranes several times to form nanoliposomes. The solution system was replaced with 5 % glucose using a Millipore ultrafiltration system (100 kDa), to which 10 mg of PX-478 was added and warmed to 60 °C for loading. The solution system was finally replaced with PBS solution (pH = 7.4) to produce folic acid modified PX-478 drug-loaded nanoliposomes, which were stored at 4 °C.

PN were characterized for zeta potential and particle size using DLS (Malvern ZetaSizer Nano ZS90, UK) and their morphology was monitored using TEM (H-600, Japan).

2.3. Synthesis of hydrogel precursors

HA-PBA was synthesized following the reported method. Briefly, 200 mg of hyaluronic acid was dissolved in 20 mL of ultrapure water with continuous stirring. Then, 200 mg of 4-(4,6-Dimethoxy1,3,5-triazin-2-yl)-4-methylmorpholinium chloride and 100 mg of 3-Aminomethylphenyl boronic acid hydrochloride were added to the hyaluronic acid solution and the pH was made to about 7. After incubating and stirring for 72 h at room temperature with a magnetic stirrer, the mixture was ultrafiltrated over membranes with a molecular weight cut-off of 6–8 kDa for 72 h. Subsequently, the reaction product was freeze-dried to give a white sponge-like product.

2.4. Preparation of the PN@MHV hydrogels

Freeze-dried HA-PBA was dissolved in analytically pure water and dosed to 10 mL volume. MHV hydrogels can be formed by mixing equal volumes of MYT solution (20 mg/mL), PVA solution (10 % w/v), and HA-PBA solution. PN were added to the MYT solution with sufficient oscillation (1.2 mM of PX-478) and then mixed with other precursors to obtain PN@MHV hydrogels.

2.5. Characterization of the PN@MHV hydrogels

The morphological aspects of the hydrogel cross-section were observed by SEM (Hitachi, SU3500) after freeze-drying the hydrogel. Before measurements, the lyophilized hydrogel samples were cut off with a knife and the cross sections were sprayed with gold.

The lyophilized hydrogel samples were grinded to powder in liquid nitrogen. The FT-IR spectra of HA-PBA, PVA, MYT, and MHV hydrogels were recorded using an FT-IR spectrometer (Thermo Fisher Scientific, Nicolet iS20).

After weighing the freeze-dried hydrogel samples to obtain the initial weight (W_0), the samples were immersed in sufficient amount of PBS and incubated at 37 °C. The humidity weight (W_i) of the swollen hydrogels was recorded at the indicated time points and the ratio of swelling was determined using the formula: Swelling ratio (%) = $((W_i - W_0)/W_0) \times 100$ %.

Mechanical tests for the freshly prepared hydrogels were carried out using a universal material testing machine (MTS, CMT6103). For the compression test, the prepared hydrogel samples were cut into cylindrical shapes with a diameter of 5 mm and a height of 5 mm, and the compression speed was 1 mm/min. The elastic modulus in compression was calculated from the slope over the linearity region (10–20 % strain) of the stress-strain curves.

2.6. Cell culture

BMSCs were obtained from the femoral and tibial bone marrow cavities of six-week-old C57BL/6 mice and cultured in DMEM/F-12 medium. RAW264.7 were purchased from China Center for Type Culture Collection and cultured in DMEM medium. All the cells were cultured at 37 °C with a 5 % CO_2 atmosphere, and the medium was refreshed every three days. To investigate the effect of HG, the culture medium containing a concentration of 40 mM glucose was used.

2.7. Osteogenic induction and evaluation of osteoblast differentiation

BMSCs were cultured to 80 % confluence and then the basal medium was replaced with DMEM/F-12 medium containing ascorbic acid (50 μg/mL), dexamethasone (10 nM), and β-glycerol phosphate (10 mM). The medium was refreshed every three days.

After 7 and 21 days of osteogenic induction, samples were fixed in 4 % formaldehyde for 20 min. The samples were then stained using the BCIP/NBT alkaline phosphatase kit (Beyotime) and Alizarin Red Kit (Cyagen) respectively. Micro images after staining were used to assess osteogenic features.

2.8. Measurement of lactate production, glucose consumption, and ATP level

In measuring the consumption of glucose and production of lactate, the initial glucose and lactate concentrations of the medium and the glucose and lactate concentrations after 24 h of incubation with osteoblasts were determined using the Glucose Assay Kit (Biovision) and the Lactate Assay Kit (Biovision), respectively.

ATP levels were measured by the Glycolysis/OXPHOS Assay kit (Dojindo). Following the kit instructions, replace the medium with fresh medium 3 h before measurement and oligomycin (1 μM) was added to inhibit mitochondrial OXPHOS and 2-DG (25 mM) was added to inhibit cellular glycolysis. Total glycolytic ATP generation was calculated by subtracting the amount of ATP in 2-DG-treated cells from the amount of ATP in untreated cells. At the end of the assay, total cellular proteins were determined using the BCA kit (Vazyme biotech) for normalization.

2.9. Cellular uptake study

RAW264.7 cells and BMSCs were vaccinated into 24-well plates as 2

× 10 ^4 per well. LPS (1 μg/mL) was added and incubated for 24 h to induce M1 macrophage polarization. RAW264.7 cells or BMSCs were incubated with FITC-labelled PN (80 μM PX-478) for 6 h (RAW264.7 cells were pre-treated with 5 mg/mL free folic acid for 2 h). Cells were then flushed with PBS 3 times. Samples were immobilized with 4 % paraformaldehyde for 20 min and stained with phalloidin-Rhodamine probe for 60 min followed by staining with DAPI for 10 min. Finally, the samples were observed and photographed using a fluorescence microscope.

In addition, flow cytometry (BD FACSCelesta) was used to quantify the active targeting of PN. RAW264.7 cells were inoculated in 6-well plates as 2 × 10 ^6 per well, pre-treated with free folic acid (5 mg/mL) for 2 h after LPS treatment to block folate receptors, and then incubated with FITC-labelled PN for about 4 h. After rinsing 3 times with PBS, the fluorescence intensity of FITC was assessed by flow cytometry.

2.10. Biocompatibility evaluation

The cytocompatibility of the hydrogels was assessed by CCK-8 assay (Biosharp) and live/dead staining. BMSCs were vaccinated into 96-well plates as 2 × 10 ^3 per well. On days 1, 3, and 5 of incubation of BMSCs with hydrogel extracts, the cell viabilities were detected by CCK-8 assay. Cell morphology was observed under a fluorescence microscope after performing live/dead staining.

The blood compatibility of the hydrogels was assessed by hemolysis assay. After the rats were anesthetized, fresh blood was collected from the heart and anticoagulated with heparin, washed five times with PBS and then centrifuged at a speed of 1200 rpm for 7 min. 200 μl of hydrogels, PBS and distilled water were co-cultured with 800 μl of erythrocytes for 6 h at 37 °C. The erythrocyte suspensions of all groups were then centrifuged at 1200 rpm for 5 min and 80 μL of supernatant from all samples was removed to a 96-well plate. The absorbance was measured at 540 nm. The hemolysis ratio was computed using the following formula: Hemolysis ratio (%) $=(OD_i\text{-}OD_p)/(OD_w\text{-}OD_p) \times 100$ %. OD_i: the OD values of each group of the samples, OD_p: the average OD value of the PBS group, OD_w: the average OD value of the distilled water group.

2.11. Intracellular ROS measurement

BMSCs were vaccinated into 96-well plates as 2 × 10 ^3 per well, incubated under HG for 2 days to induce ROS production, and intervened with hydrogel extracts. The ROS probe DCFH-DA (10 μM in FBS-free medium, Beyotime) was added to all groups as well as incorporated at 37 °C for 20 min and observed by fluorescence microscopy. The relative level of intracellular ROS was calculated by fluorescence intensity.

2.12. RT-PCR assay

Total cellular RNA was extracted with TRIzol (Invitrogen) kit according to the instructions, and then reverse transcribed into cDNA following the PrimeScript cDNA synthesis kit (Vazyme biotech). RT-PCR was conducted using a Bio-Rad CFX96 system and data were analyzed using the 2^(-ΔΔCt) method. Oligonucleotide primers for RT-PCR are listed below.

Primer sequences used:

β-actin (Forward: 5′-CATCCGTAAAGACCTCTATGCCAAC-3’; Reverse: 5′-ATGGAGCCACCGATCCACA-3′); HIF-1α (Forward: 5′-ACCTTCATCGGAAACTCCAAAG-3’; Reverse: 5′-CTGTTAGGCTGGGAAAAGTTAGG-3′); GLUT1 (Forward: 5′- CAGTTCGGCTATAACACTGGTG-3’; Reverse: 5′- GCCCCCGACAGAGAAGATG-3′); HKII (Forward: 5′-TGATCGCCTGCTTATTCACGG-3’; Reverse: 5′- AACCGCCTAGAAATCTCCAGA-3′); PDK1 (Forward: 5′-GGACTTCGGGTCAGTGAATGC-3’; Reverse: 5′-TCCTGAGAAGATTGTCGGGGA-3′); PFK1 (Forward: 5′-TGTGGTCCGAGTTGGTATCTT-3’; Reverse: 5′- GCACTTCCAATCACTGTGCC-3′); LDHA (Forward: 5′-TGTCTCCAGCAAAGACTACTGT-3’; Reverse: 5′-GACTGTACTTGACAATGTTGGGA-3′); ALP (Forward: 5′-CCAACTCTTTTGTGCCAGAGA-3’; Reverse: 5′- GCTACATTGGTGTTGAGCTTTT-3′); RUNX2 (Forward: 5′-ATGCTTCATTCGCCTCACAAA-3’; Reverse: 5′-GCACTCACTGACTCGGTTGG-3′); COL1A1 (Forward: 5′-GCTCCTCTTAGGGGCCACT-3’; Reverse: 5′- CCACGTCTCACCATTGGGG-3′); OCN (Forward: 5′-CTGACCTCACAGATCCCAAGC-3’; Reverse: 5′-TGGTCTGATAGCTCGTCACAAG-3′); IL-1β (Forward: 5′-AAGCTGATGGCCCTAAACAG-3’; Reverse: 5′-AGGTGCATCGTGCACATAAG-3′); TNF-α (Forward: 5′-CCGAGGCAGTCAGATCATCTT-3’; Reverse: 5′- AGCTGCCCCTCAGCTTGA-3′); IL-10 (Forward: 5′- CCAAGCCTTATCGGAAATGA-3’; Reverse: 5′- TTTTCACAGGGGAGAAATCG-3′); TGF-β (Forward: 5′-CTCCCGTGGCTTCTAGTGC-3’; Reverse: 5′- GCCTTAGTTTGGACAGGATCTG-3′).

2.13. Western blots analysis

Protein expression levels were determined by Western blots. Cells were rinsed several times with cold PBS, lysed by ultra-sonication in RIPA buffer with the addition of a protease inhibitor (MCE), and then centrifuged to extract the supernatant. Determination of protein content was carried out using a BCA kit (Vazyme biotech). Protein samples were prepared by mixing thoroughly with sample loading buffer and heating at 95 °C over a period of 5 min. Then, ~30 μg of total protein per group was fractionated by electrophoresis on 12.5 % SDS-PAGE and later, it was transferred to PVDF membranes by electroblotting. The membranes were incubated with 5 % (w/v) skimmed milk for 2 h at room temperature to encapsulate the membranes, then incubated with primary antibody overnight at 4 °C. Subsequently, the membranes were incubated with the horseradish peroxidase-coupled anti-rabbit antibody at room temperature and shaken on a shaker for 1 h, and then visualized with an enhanced chemiluminescence detector system (Bio-Rad). Quantitative analysis of grey values from western blots was performed with ImageJ software.

2.14. Flow cytometry

RAW264.7 cells were vaccinated into 6-well plates as 2 × 10 ^6 per well. To assess macrophage polarization, RAW264.7 cells were treated with PE-labelled CD86 antibody (to mark M1 macrophages) and PERCP-labelled CD206 antibody (to mark M2 macrophages) sequentially according to the method provided from the antibody manufacturer. The polarization profile of the cells was then analyzed by flow cytometry.

2.15. T2D mice fracture model

C57BL/6J male mice (n = 54; aged 6 weeks) were purchased from BIONT Biological Technology Company (Wuhan, China). All experiments were performed in accordance with the guidelines of the Animal Care and Use Committee at Tongji Medical College, Huazhong University of Science and Technology.

For T2D induction, 6-week-old C57BL/6 J male mice were fed a high-fat diet (HFD) with 60 kcal% fat for 4 weeks and then injected intraperitoneally with streptozotocin (40 mg/kg, freshly prepared in citric acid/sodium citrate buffer, pH = 4.5) once a day for 3 consecutive days (with a 5 h fast before injection). Glucose levels in tail vein blood were randomly determined 5 days after injection using a glucometer (One-Touch SureStep Plus, Lifescan). Mice with blood glucose concentrations over 300 mg/dL were designated as appropriate T2D animal models and continued HFD until the end of the experiment.

After anesthesia by intraperitoneal injection, a longitudinal incision of 5 mm was made in the right thigh of the mouse under sterile conditions. The muscles were incrementally and obtrusively separated until the femur was completely exposed. A 25 G syringe needle was used as an intramedullary fixation device and inserted retrogradely into the marrow cavity of the femur. Transverse fractures of the femur were

made using water-jawed forceps. Hydrogel was placed at the femoral fracture site and the incision was closed layer by layer. Mice were anesthetized for X-ray imaging on days 7, 14 and 21 after surgery. Mice were executed on days 14 and 21 after surgery, and the femur was removed and immersed in 4 % formalin for fixation.

2.16. X-ray imaging and micro-CT analysis

For X-ray images, the mice were anesthetized and then subjected to 5 s of X-ray irradiation at 32 kV (Faxitron X-Ray).

The isolated femur was scanned using micro-CT (U-CT-XUHR, MILabs) with a resolution of 10.5 μm and 55 kVp. The 3D structure of the calcaneus was reconstructed by the CT-VOX version 2.1 software and analyzed by the microcomputed tomography software CTAN version 1.12 software. Bone and tissue volumes in the vicinity of the fracture site were assessed to calculate BV, TV, and BV/TV. Samples were then decalcified with 0.5 M EDTA for 3 weeks.

2.17. Histological analysis

After decalcification, the bone tissue was embedded in wax to cut sections of 6 μm thickness. Sections of the samples were stained with Masson's trichrome and H&E to evaluate the bone healing. Immunohistochemistry and immunofluorescence staining were used for determining the expression of protein.

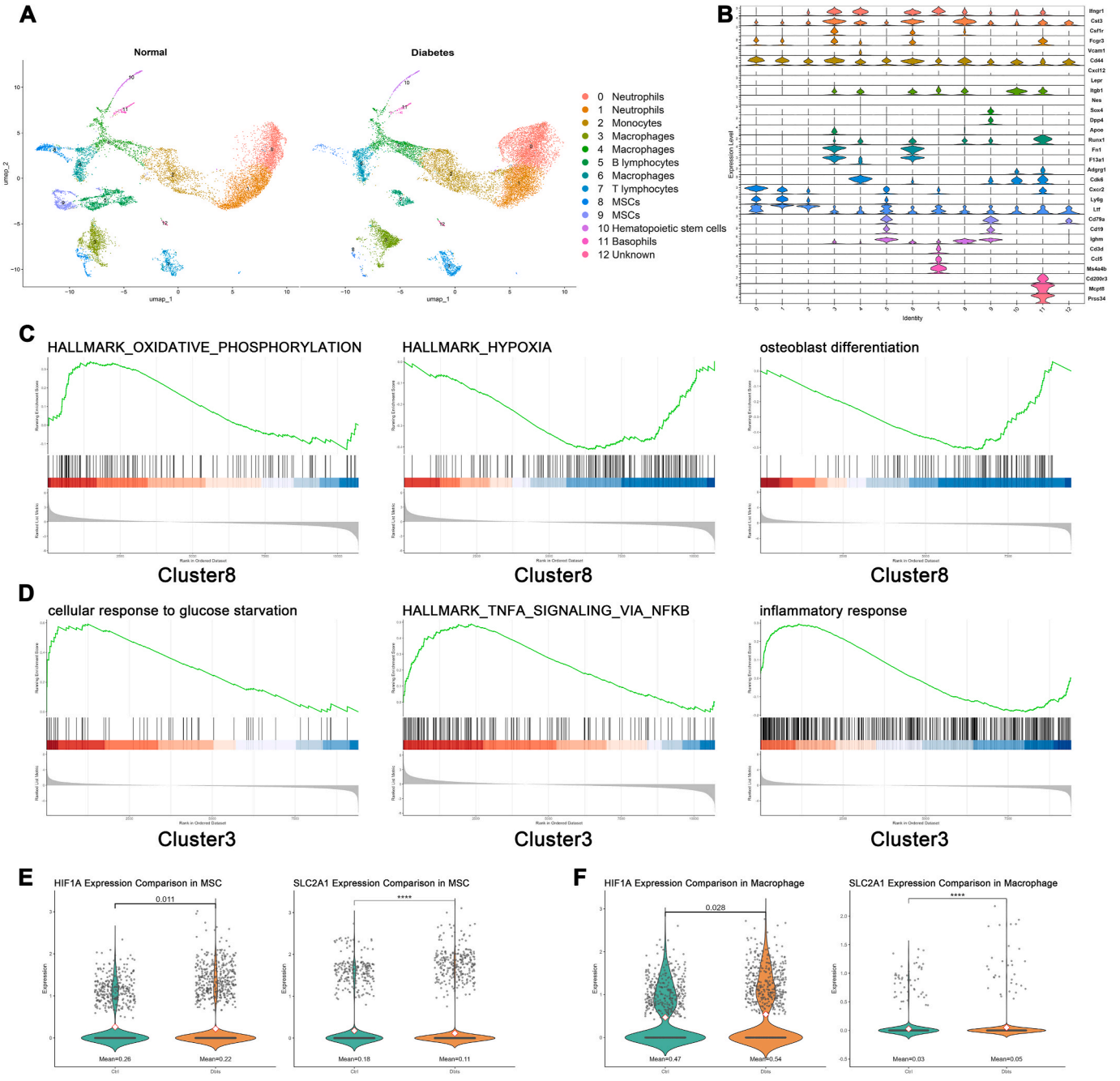

Fig. 2. Diabetes affects glucose metabolism and cellular function of BMSCs and macrophages from bone marrow. (A) UMAP clusters with annotations to the right. (B) Violin plots of the representative molecular markers used for cluster annotation. (C, D) GSEA graphs of diabetes over normal for indicated clusters. (E) Violin plots of HIF1A and SLC2A1 genes in MSCs of normal and diabetic mice. (F) Violin plots of HIF1A and SLC2A1 genes in macrophages of normal and diabetic mice.

2.18. Single-cell RNA-sequencing data processing and analysis

The single-cell RNA-sequencing dataset of mouse bone marrow (GEO: GSE182986) was extracted from the Gene Expression Omnibus (GEO) database [29]. Quality control and preprocessing of data was performed using various R and Bioconductor packages. Low-quality cells (genes <200, >25 % mitochondrial genes) and genes only uniquely expressed in <3 cells in the dataset were filtered. After principal

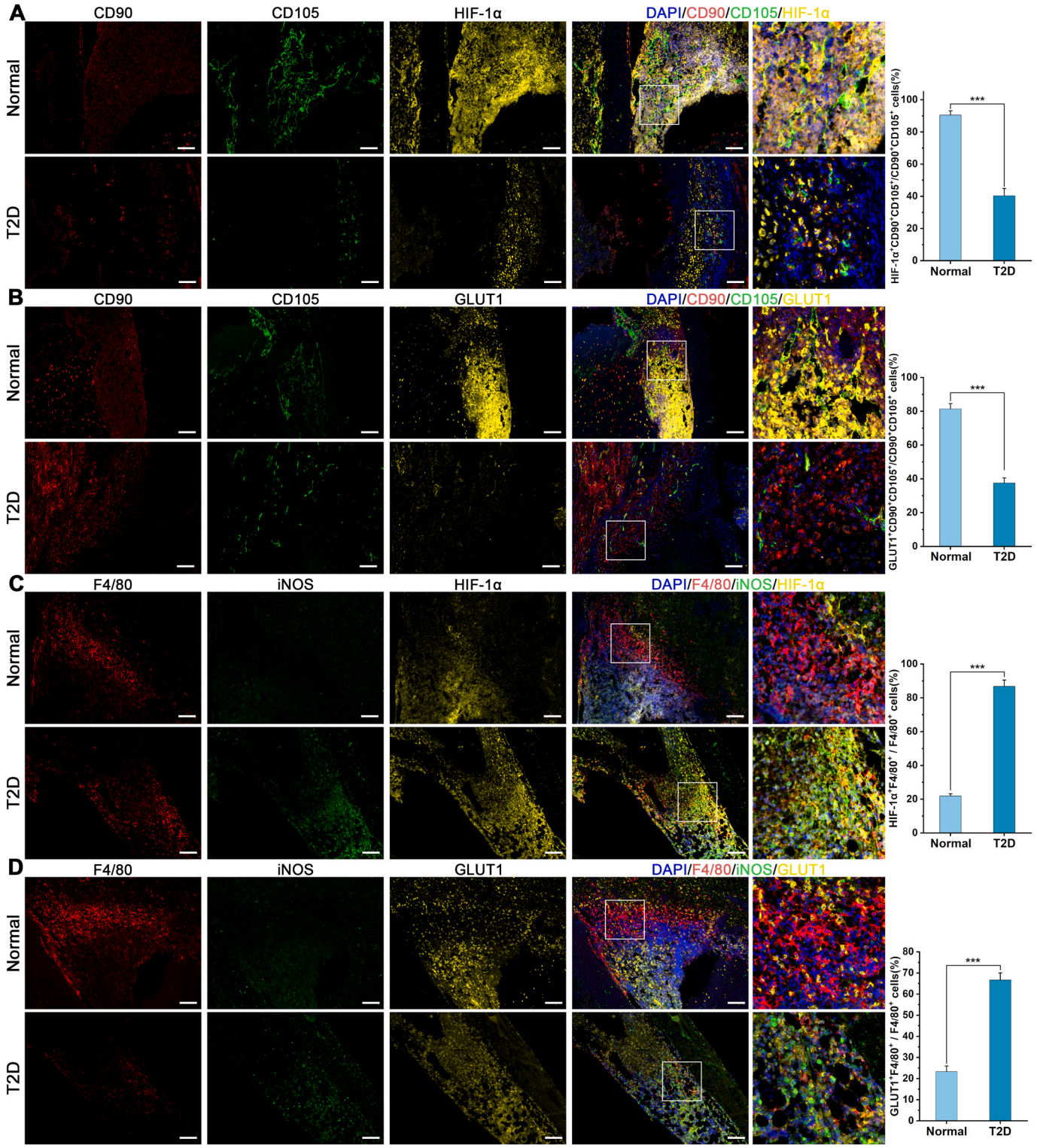

Fig. 3. Abnormal glycolysis in BMSCs and macrophages during fracture healing in T2D mice. (A) Immunofluorescence staining and quantitative analysis of DAPI, CD90, CD105, and HIF-1α at the fracture site on day 7 after femur fracture. (B) Immunofluorescence staining and quantitative analysis of DAPI, CD90, CD105, and GLUT1 at the fracture site on day 7 after femur fracture. (C) Immunofluorescence staining and quantitative analysis of DAPI, F4/80, iNOS, and HIF-1α at the fracture site on day 7 after femur fracture. (D) Immunofluorescence staining and quantitative analysis of DAPI, F4/80, iNOS, and GLUT1 at the fracture site on day 7 after femur fracture. Scale bar = 100 μm. All quantitative data are represented as mean ± SD (n = 3 independent animals, *p < 0.05, **p < 0.01, ***p < 0.001).

component analysis, dimensionality reduction was performed using UMAP. Differentially expressed genes were identified using the FindAllMarkers function. Gene set enrichment analysis (GSEA) was performed using MsigDB gene sets and Gene Ontology (GO) function enrichment analysis to identify significantly affected pathways. Expression levels of the indicated genes were visualized using VlnPlot function of Seurat.

2.19. Statistical analysis

Statistical analysis was carried out using SPSS 26.0 software. The data all represent the results from minimum three independent experiments, and are expressed as mean ± SD. Comparisons between two groups of data were made utilizing the two-tailed Student's t-test. In all statistical tests, a value of $P \leq 0.05$ was classified as being significant.

3. Result

3.1. Diabetes affects glucose metabolism and cellular function of BMSCs and macrophages from bone marrow

We analyzed single-cell RNA-sequencing data from bone marrow of normal and diabetic mice. A total of 13 cell clusters were identified after unsupervised cluster analysis (Fig. 2A). We annotated each cluster by specific marker genes that were significantly expressed in the cells: MSCs (mainly expressing Cd44, Cxcl12, Lepr, Nes, and Runx1), macrophages (mainly expressing Ifngr1, Csf1r, Fcgr3, and Vcam1), monocytes (mainly expressing Fn1 and F13a1), basophils (mainly expressing Cd200r3, Mcpt8, and Prss34), neutrophils (mainly expressing Cxcr2, Ly6g, and Ltf), hematopoietic stem cells (mainly expressing Adgrg1 and Cdk6), T lymphocytes (mainly expressing Cd3d, Ccl5, and Ms4a4b) and B lymphocytes (mainly expressing Cd79a, Cd19, and Ighm) (Fig. 2A and B). The MSCs were comprised of clusters 8 and 9, with cluster 9 highly expressing stemness genes Sox4 and Dpp4 (Fig. 2B). Notably, MSC cluster 9 almost disappeared in diabetic mice compared to normal mice, suggesting that diabetes affects the stemness of BMSCs (Fig. 2A).

GSEA against MSCs and macrophages showed that in MSC cluster 8 of diabetic mice, oxidative phosphorylation pathway was upregulated, and hypoxia pathway and osteoblast differentiation pathway were suppressed (Fig. 2C). On the other hand, glucose starvation, TNFA signaling, and inflammatory response pathway were upregulated in macrophage cluster 3 of diabetic mice (Fig. 2D). Analysis of genes revealed that HIF1A (the gene encoding HIF-1α) and SLC2A1 (the gene encoding GLUT1) genes were upregulated in macrophages from diabetic mice (Fig. 2F), and HIF1A and SLC2A1 genes were downregulated in MSCs (Fig. 2E). These suggest that diabetes affects glucose metabolism and cellular function of macrophages and MSCs in bone marrow.

3.2. Abnormal glycolysis in BMSCs and macrophages in T2D fracture healing

BMSCs were labelled with CD90 and CD105 surface markers by immunofluorescence staining to distinguish them [30]. A significant reduction in BMSC populations within the bone microenvironment of T2D mice was observed on day 7 post-fracture (Fig. 3A and B). Immunostaining of HIF-1α revealed a marked decrease in HIF-1α expression in BMSCs from T2D mice (Fig. 3A). Given that GLUT1 is the main glucose transporter in osteoblasts and is transcriptionally regulated by HIF-1α, [31,32], we observed diminished GLUT1 expression in BMSCs from T2D mice (Fig. 3B), suggesting impaired glycolysis, which may hinder osteoblast differentiation. Simultaneously, we identified proinflammatory M1 macrophages via immunofluorescence staining of F4/80 and inducible nitric oxide synthase (iNOS) (Fig. 3C and D). The data showed elevated levels of iNOS in $F4/80^{+}$ cells within the bone microenvironment of T2D mice compared to normal group, indicating an increased population of proinflammatory M1 macrophages on day 7 post-fracture. Immunostaining of HIF-1α also demonstrated increased expression in these macrophages, along with higher GLUT1 levels (Fig. 3C and D), suggesting enhanced glycolysis. These findings highlight dysregulated glycolysis during the early phase of fracture healing in T2D mice, characterized by suppressed glycolysis in BMSCs and elevated glycolysis in proinflammatory M1 macrophages.

3.3. MYT alleviates the inhibitory effect of high glucose environment (HG) on HIF-1α-mediated glycolysis in BMSCs

To assess the optimal concentration of MYT for cells, we evaluated cell viability after 3 days of treatment with different concentrations of MYT by CCK-8 assay. No significant difference in cell viability was observed at concentrations below 100ug/mL, while concentrations above 100ug/mL resulted in significant toxicity (Fig. 4A). Therefore, we chose 50ug/mL for subsequent experiments. HG is a major contributor to cell and tissue damage in diabetic patients, inducing ROS overproduction [33,34]. HG affects the survival, proliferation and differentiation of osteoblasts [35,36]. Western blots and RT-PCR showed that MYT restored the expression of HIF-1α and GLUT1, which were downregulated under HG (Fig. 4B, C, F). Furthermore, key glycolytic genes, including hexokinase II (HKII), phosphofructokinase 1 (PFK1), and lactate dehydrogenase A (LDHA), were suppressed by HG but were restored by MYT treatment (Fig. 4E). Pyruvate dehydrogenase kinase 1 (PDK1) inhibits mitochondrial respiration and promotes glycolysis by preventing pyruvate entry into the TCA cycle. We observed that PDK1 expression followed a pattern similar to that of HIF-1α under HG and after MYT treatment (Fig. 4E, F, S1). Osteoblast differentiation is accompanied by enhanced aerobic glycolysis [20]. To assess glycolytic activity, we measured the rate of glucose consumption, the rate of lactate production, and ATP production at days 3, 7, and 14 of differentiation. It was found that the rate of glycolysis gradually increased and stabilized during osteoblast differentiation, that HG inhibited this process, on the other hand, MYT alleviated the inhibition of glycolysis under HG (Fig. 4G). The contribution of glycolysis to ATP production was reduced under HG but restored by MYT (Fig. 4H). Given the important interaction between GLUT1 and RUNX2, suppression of GLUT1 may affect RUNX2 expression and impair osteoblast differentiation [31]. We found that RUNX2 changed similarly to HIF-1α-glycolysis with the intervention of HG and MYT (Fig. 4D, F). These results suggest that MYT alleviates HG-induced impairment of glycolysis and osteoblast differentiation.

3.4. MYT promotes osteoblast differentiation by enhancing glycolysis under HG

RUNX2, a key regulator and marker of osteoblast differentiation, was positively influenced by MYT. To evaluate the effects of HG on osteoblast differentiation of BMSCs and the role of MYT treatment, we examined the expression of osteoblast marker genes. Under HG, expression of osteoblast marker genes (ALP, COL1A1, and OCN) in BMSCs was significantly reduced, but MYT treatment notably increased their expression (Fig. 5A). Furthermore, ALP staining and Alizarin Red staining conducted after 7 and 21 days of osteogenic induction demonstrated that HG suppressed ALP activity and mineralized nodule formation, effects that were reversed by MYT (Fig. 5B and C). These findings underscore the positive role of MYT in promoting osteoblast differentiation under HG.

To elucidate whether MYT enhances BMSC osteoblast differentiation by augmenting glycolysis under HG, we inhibited glycolysis using 2-deoxy-D-glucose (2-DG, 1 mM) during osteogenic induction [37]. RT-PCR analysis indicated that glycolysis inhibition during MYT treatment led to a suppression of osteoblast marker gene expression (Fig. 5D). ALP staining on day 7 and Alizarin Red staining on day 21 of osteogenic induction confirmed that glycolysis inhibition resulted in decreased ALP activity and a reduction in the accumulation of mineralized nodules

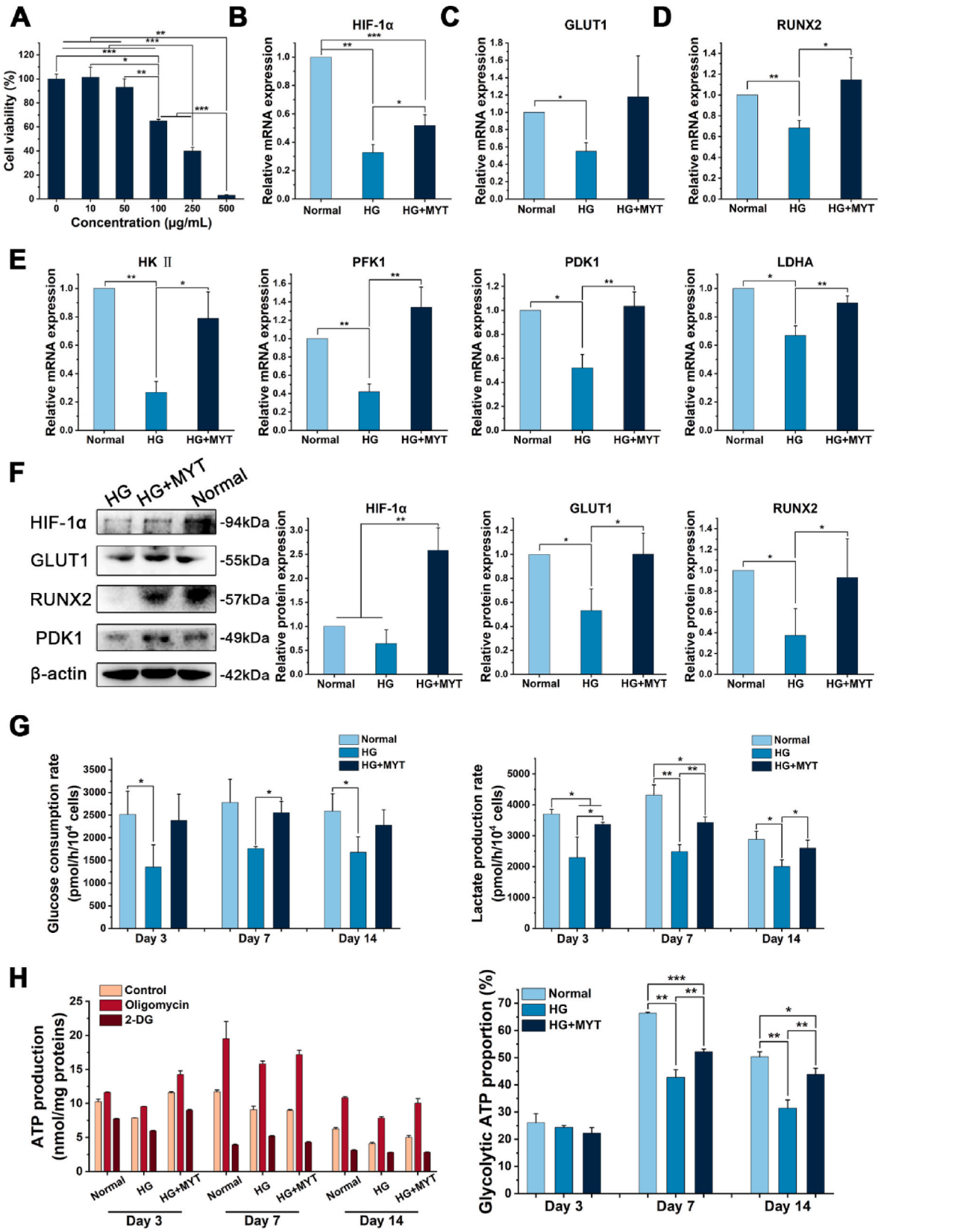

Fig. 4. MYT alleviates the effect of HG on cellular glycolysis during osteoblast differentiation. (A) Viability of BMSCs determined by CCK-8 assay after incubation with different concentrations of MYT for 72 h. (B-E) Expression of HIF-1α, GLUT1, RUNX2, and other glycolytic genes in BMSCs detected by RT-PCR after 48 h of treatment. (F) Western blots of HIF-1α, GLUT1, RUNX2, PDK1, and β-actin in BMSCs, and quantitative analysis of HIF-1α, GLUT1, and RUNX2 after 72 h of treatment. (G) Glucose consumption rate and lactate production rate in BMSCs after osteogenic induction for 3, 7, and 14 days. (H) Levels of ATP in BMSCs after osteogenic induction for 3, 7, and 14 days, and the proportion of glycolytic ATP to total ATP. All quantitative data are represented as mean ± SD (n = 3, *p < 0.05, **p < 0.01, ***p < 0.001).

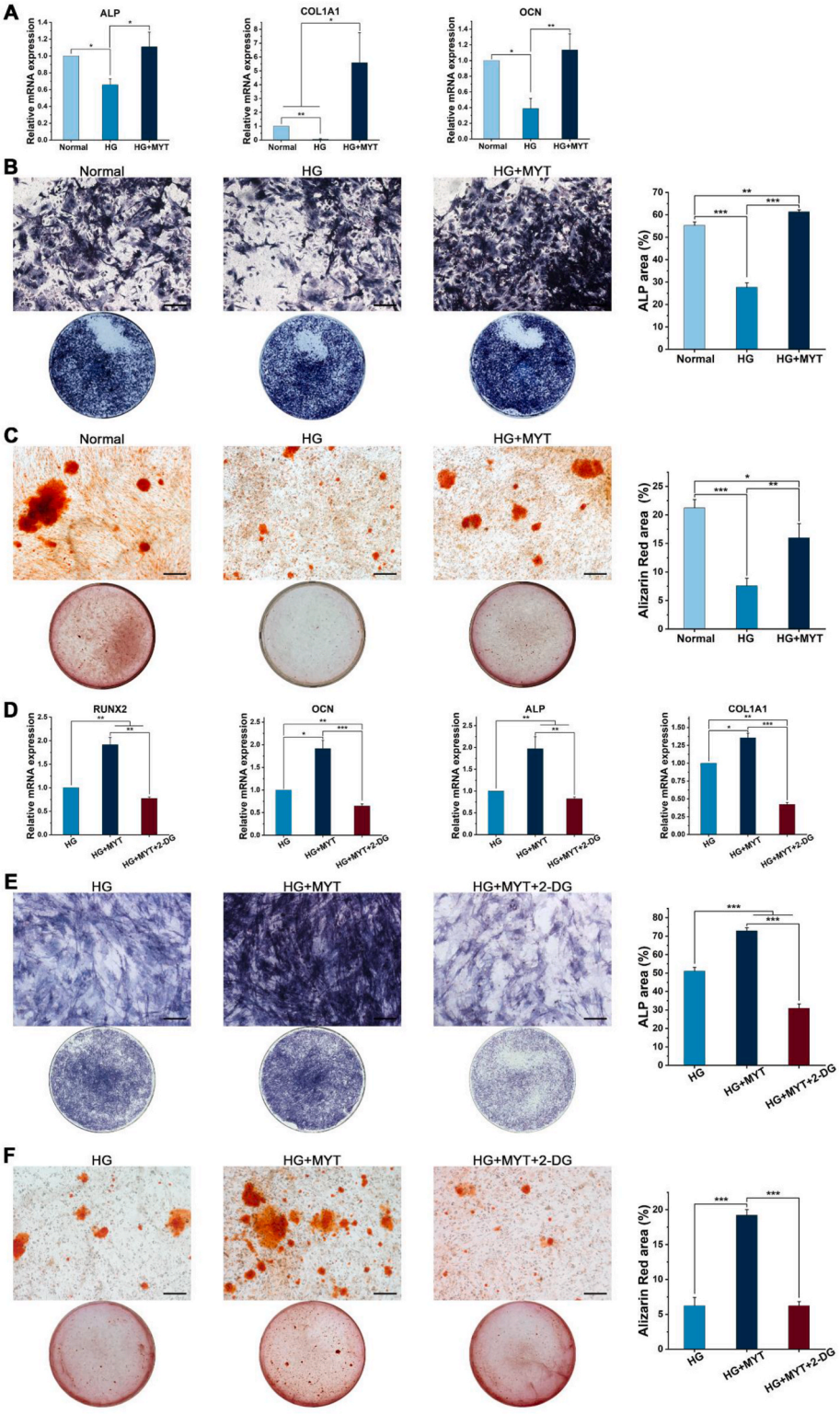

Fig. 5. MYT enhances osteoblast differentiation via promoting glycolysis under HG. (A) Expression of ALP, COL1A1, and OCN genes in BMSCs detected by RT-PCR after 48 h of treatment. (B) ALP staining of BMSCs and quantitative analysis after osteogenic induction for 7 days. (C) Alizarin Red staining of BMSCs and quantitative analysis of mineralized nodules accumulation after osteogenic induction for 21 days. (D) Expression of RUNX2, OCN, ALP, and COL1A1 genes in BMSCs detected by RT-PCR after 48 h of treatment. (E) ALP staining of BMSCs and quantitative analysis after osteogenic induction for 7 days. (F) Alizarin Red staining of BMSCs and quantitative analysis of mineralized nodules accumulation after osteogenic induction for 21 days. Scale bar = 100 μm. All quantitative data are represented as mean ± SD (n = 3, *p < 0.05, **p < 0.01, ***p < 0.001).

(Fig. 5E and F). Thus, the inhibition of glycolysis effectively blocked the promotion of BMSC osteoblast differentiation by MYT under HG. Collectively, these results suggest that MYT promotes osteoblast differentiation by enhancing glycolysis in BMSCs under HG.

3.5. Preparation and characterization of PN@MHV hydrogel

PX-478, a specific inhibitor of HIF-1α [28], was loaded into liposomal nanoparticles with folic acid attached (PN) to target M1 macrophages, which overexpress folate receptors [38]. Transmission electron microscopy (TEM) images confirmed the spherical shape and uniform size of the nanoparticles (Fig. 6B) while dynamic light scattering (DLS) measurements revealed a hydrodynamic diameter of 80–200 nm (Fig. 6C), and the zeta potential was approximately −25 mV (Fig. 6D). Hydrogels have excellent stability, drug encapsulation efficiency and biocompatibility. Since MYT has multiple hydroxyl groups, we hypothesized that extensive hydrogen bond interactions could be generated among MYT, HA-PBA, and PVA leading to the formation of hydrogels. We mixed different concentrations of MYT with HA-PBA, PVA solutions to form MHV hydrogels. The swelling ratio of the hydrogels increased with rising MYT concentration, reaching a peak at 20 mg/mL (Fig. S2A), which was chosen for subsequent experiments.

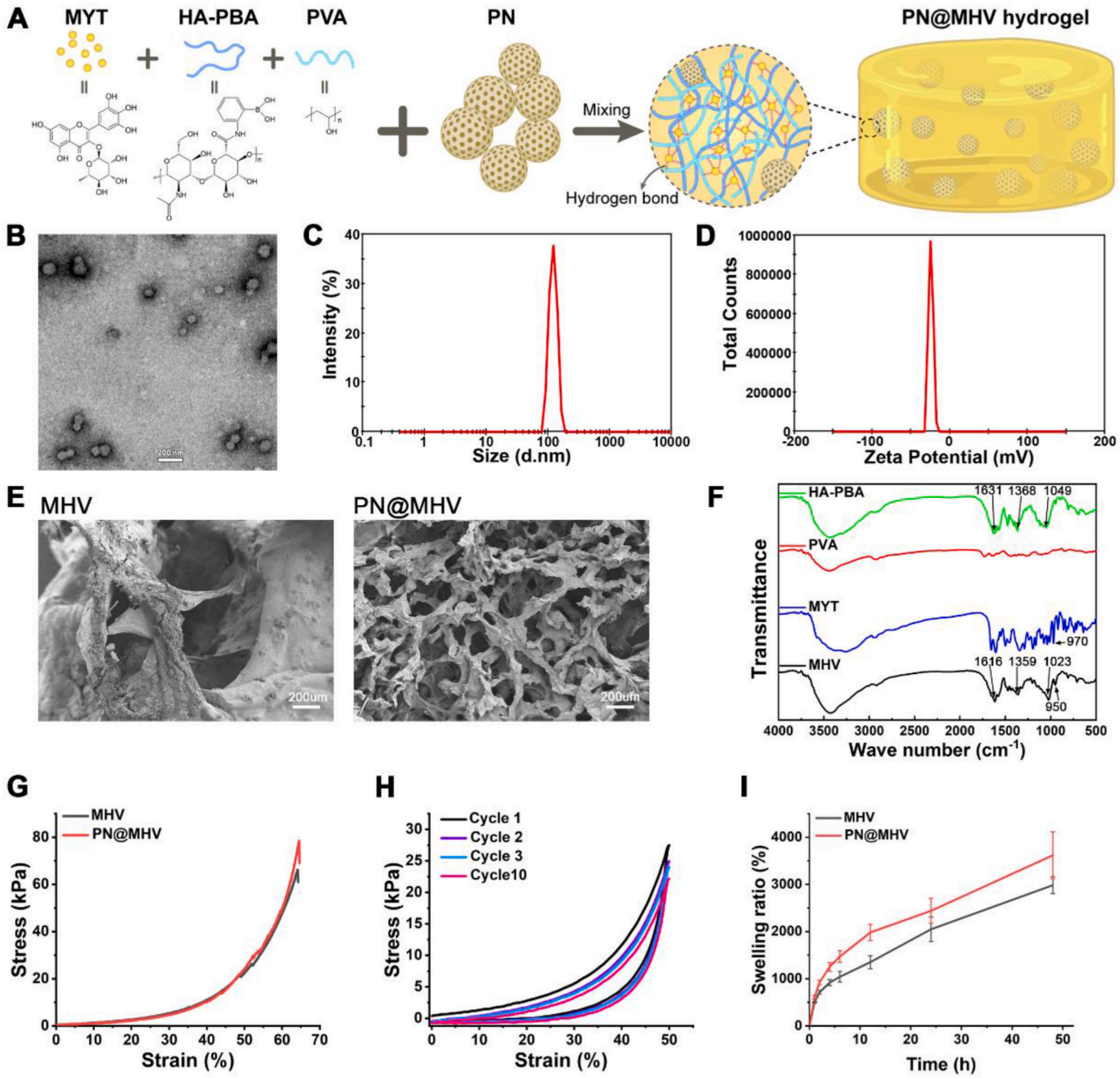

Fig. 6. Characterization of nanoparticles and hydrogels. (A) Schematic illustration of the chemical structures of the hydrogel precursors and the preparation of PN@MHV hydrogel. (B) TEM image of nanoparticles. (C) Particle size distribution of nanoparticles. (D) Zeta potential distribution of nanoparticles. (E) SEM images of MHV and PN@MHV hydrogels. (F) FT-IR spectra of HA-PBA, PVA, MYT, and MHV hydrogel. (G) Compressive stress–strain curves of MHV and PN@MHV hydrogels. (H) Cyclic compressive stress–strain curves of the PN@MHV hydrogel. (I) Swelling curves of MHV and PN@MHV hydrogels incubated in PBS at 37 °C (n = 3, data are represented as mean ± SD).

Observation of freeze-dried hydrogel cross-sections by scanning electron microscopy (SEM) showed that both MHV and PN@MHV hydrogels formed a porous network structure (Fig. 6E).

We analyzed the molecular interactions in the hydrogels by Fourier transform infrared (FT-IR) spectra (Fig. 6F). In the spectrum of HA-PBA, the characteristic peak for amide I band (C=O) at 1631 cm^{-1}, the characteristic peak for B-O bond at 1368 cm^{-1}, and the characteristic peak for C-O-C at 1049 cm^{-1} were observed. MYT is a type of flavonoid glycosides, and in its spectrum the characteristic peak for glycosidic bond was observed at 970 cm^{-1}. In the spectrum of MHV hydrogel, the characteristic peaks for amide I band, B-O bonds, C-O-C, and glycosidic bond were observed and respectively shifted from 1631 cm^{-1} to 1616 cm^{-1}, from 1368 cm^{-1} to 1359 cm^{-1}, from 1049 cm^{-1} to 1023 cm^{-1}, and from 970 cm^{-1} to 950 cm^{-1} in comparison to the absorption peaks of HA-PBA and MYT. The presence of characteristic peaks from MYT in the MHV spectrum indicated the successful introduction of MYT into the hydrogel. The slight red shift of the characteristic peaks indicated the formation of hydrogen bonds between MYT, HA-PBA, and PVA leading to the formation of hydrogel.

We cultured BMSCs with PN@MHV hydrogels containing different concentrations of PX-478 for 3 days and then performed CCK-8 assay (Fig. S2B). Cell viability was not significantly inhibited below the concentration of 1.2 mM, therefore the concentration of 1.2 mM was chosen for PN@MHV hydrogel preparation.

We characterized the mechanical properties of the hydrogels by compression experiments. As shown in the compressive stress-strain curves (Fig. 6G), the MHV and PN@MHV hydrogels broke at about 63 % strain, and there was no significant difference in the elastic modulus between MHV and PN@MHV hydrogels (Fig. S2C), indicating that the incorporation of PN has no obvious effect on the mechanical properties of the MHV hydrogel. We then performed 10 rounds of continuous loading-unloading compressive cycle tests on PN@MHV hydrogels at 50 % strain. The cyclic compressive stress-strain curves showed an obvious hysteresis loop in the first loading-unloading cycle and a decline of the hysteresis loop and compressive stress after the first cycle, but the decline of the hysteresis loop and compressive stress from the 2nd cycle to the 10th cycle was negligible, suggesting that the hydrogel exhibits good fatigue compressive resistance (Fig. 6H). We further examined the swelling properties of the hydrogels. The swelling rates of MHV and PN@MHV hydrogels were high within the first 8 h and reached swelling equilibrium within 48 h (Fig. 6I). The swelling ratios of MHV and PN@MHV hydrogels were 2982 % and 3617 %, respectively, indicating that the hydrogels exhibit good swelling properties that could be beneficial for fracture hemostasis. In vitro degradation analysis showed that the hydrogels could be completely degraded within 9 days (Fig. S2D). MYT and PX-478 release profiles were also recorded, as shown in Fig. S2E and Fig.S2F.

3.6. Biocompatibility, antioxidative and hemostatic effects of PN@MHV hydrogel

To evaluate the efficacy of the hydrogels, we assessed their biocompatibility and protective effects using live/dead staining, the CCK-8 assay, and a hemolysis assay. BMSCs were incubated with MHV and PN@MHV hydrogels for 1, 3, and 5 days, after which live/dead staining revealed a marked increase in the number of dead cells under HG; whereas both hydrogel treatments reduced the number of dead cells (Fig. 7A). CCK-8 assay results demonstrated no significant differences in BMSC viability between the normal group and either hydrogel group (Fig. 7B), confirming the favorable cytocompatibility of both hydrogels. Furthermore, in the hemolysis assay, negligible hemolysis was observed with both hydrogels (Fig. 7C and D), indicating excellent blood compatibility. Additionally, H&E staining of heart, liver, spleen, lung, and kidney tissues from mice treated with MHV and PN@MHV hydrogels showed no noticeable systemic damage compared to the untreated group (Fig. S3). Collectively, these findings underscore the good biocompatibility of MHV and PN@MHV hydrogels.

Given that HG induces excessive ROS production, we subsequently investigated the antioxidative capabilities of the hydrogels. Staining with the ROS probe DCFH-DA revealed an increased fluorescence intensity under HG, which was significantly diminished following treatment with MHV and PN@MHV hydrogels (Fig. 7E and F), indicating their ability to scavenge intracellular ROS. Additionally, in a mouse liver hemorrhage model, treatment with the hydrogels resulted in reduced blood loss, comparable to the commercial hemostatic agent Merocel (Fig. 7G and H), highlighting their effective hemostatic performance.

3.7. PN@MHV hydrogel promotes osteoblast differentiation of BMSCs through HIF-1α-mediated glycolysis

To evaluate the targeting capability of nanoparticles within hydrogels, BMSCs were incubated with FITC-labelled nanoparticles for 6 h. Fluorescence analysis revealed a weak FITC signal within BMSCs (Fig. 8A), suggesting a low level of non-specific nanoparticle uptake by the cells. To further assess the impact of hydrogels and macrophage-targeting nanoparticles on BMSCs, we administered extracts from MHV and PN@MHV hydrogels during the osteoblast differentiation of BMSCs under HG. Both treatments significantly increased HIF-1α expression compared to the HG group, with no significant difference between the hydrogel groups (Fig. 8B, C, S4), suggesting that non-specific nanoparticle uptake does not significantly affect BMSCs. We also assessed the effects of the hydrogels on glycolysis during osteoblast differentiation. Western blots and RT-PCR analyses showed increased GLUT1 expression in BMSCs treated with MHV and PN@MHV hydrogels (Fig. 8B, D, S4), indicating the hydrogels counteract the inhibitory effects of HG on glycolysis. Given the importance of aerobic glycolysis in osteoblast differentiation, we examined its impact on osteoblast marker expression. Both hydrogels significantly enhanced the expression of osteoblast marker genes under HG (Fig. 8B, E, S4). Additionally, ALP activity staining on day 7 and Alizarin Red staining on day 21 of osteogenic induction revealed that hydrogel intervention markedly promoted both ALP activity and the accumulation of mineralized nodules (Fig. 8F and G). These findings confirm that MHV and PN@MHV hydrogels could facilitate the osteoblast differentiation of BMSCs under HG by enhancing aerobic glycolysis.

3.8. PN@MHV hydrogel targets M1 macrophages to inhibit the HIF-1α-mediated glycolysis and exert anti-inflammatory effects

To inhibit the inflammatory function of proinflammatory M1 macrophages, we delivered the HIF-1α inhibitor PX-478 via nanoparticles (PN) to suppress cellular glycolysis and exert anti-inflammatory effects. To assess the targeting ability of surface-modified folic acid nanoparticles (labelled with FITC) for M1 macrophages, RAW264.7 cells were incubated with the nanoparticles for 6 h following LPS pretreatment for 24 h. Fluorescence imaging revealed stronger FITC signals in macrophages after LPS treatment, indicating increased nanoparticle uptake (Fig. 9A and B). To confirm that nanoparticle uptake was mediated by folic acid - folate receptor binding, we pretreated the cells with excess free folic acid to block the receptor, followed by nanoparticle addition. Flow cytometry showed significantly reduced fluorescence intensity in macrophages pretreated with free folic acid, confirming that blocking the folate receptor inhibited nanoparticle uptake (Fig. 9C and D). In contrast, for RAW264.7 cells in the control groups, there was no significant difference in cellular fluorescence intensity after free folic acid treatment (Fig. 9C and D). These results demonstrate that nanoparticles could target M1 macrophages via folate receptors.

We investigated the effects of MHV and PN@MHV hydrogel extracts on macrophage glycolysis under HG. Western blots and RT-PCR results revealed higher expression levels of HIF-1α and GLUT1 in HG-treated macrophages compared to the normal group. No significant difference

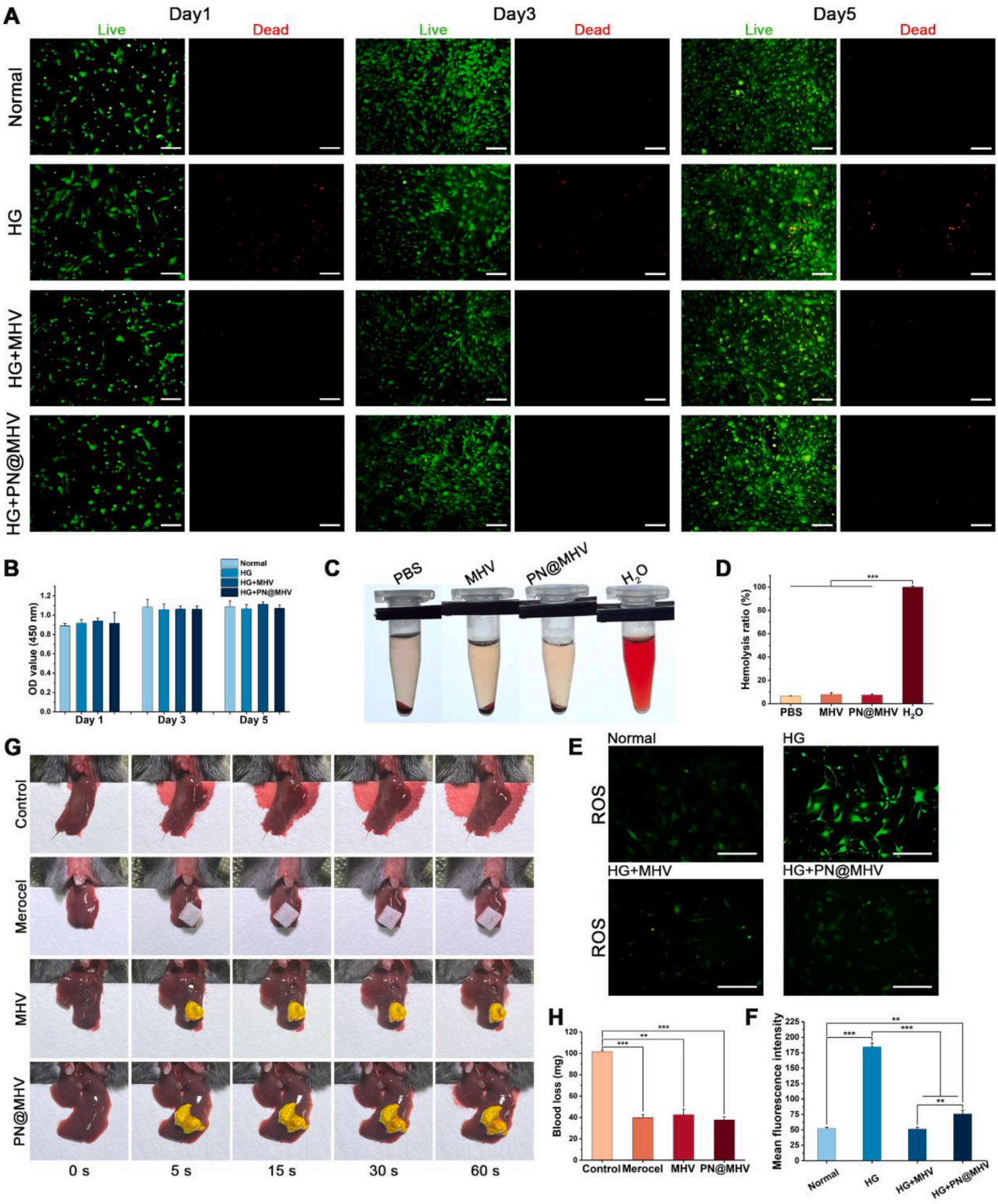

Fig. 7. Biocompatibility, antioxidative and hemostatic effects of hydrogels. (A) Calcein-AM/propidium iodide (PI) staining of BMSCs after treatment with MHV and PN@MHV hydrogels under HG for 1, 3, and 5 days. (B) CCK-8 assay of BMSCs after 1, 3, and 5 days of treatment. (C and D) Hemolysis assay for MHV and PN@MHV hydrogels. (E and F) ROS probe DCFH-DA staining of BMSCs and quantitative analysis after 48 h of treatment. (G and H) Mouse liver hemorrhage model and quantitation of blood loss for hemostatic effect evaluation. Scale bar = 100 μm. All quantitative data are represented as mean ± SD (n = 3 independent animals, *p < 0.05, **p < 0.01, ***p < 0.001).

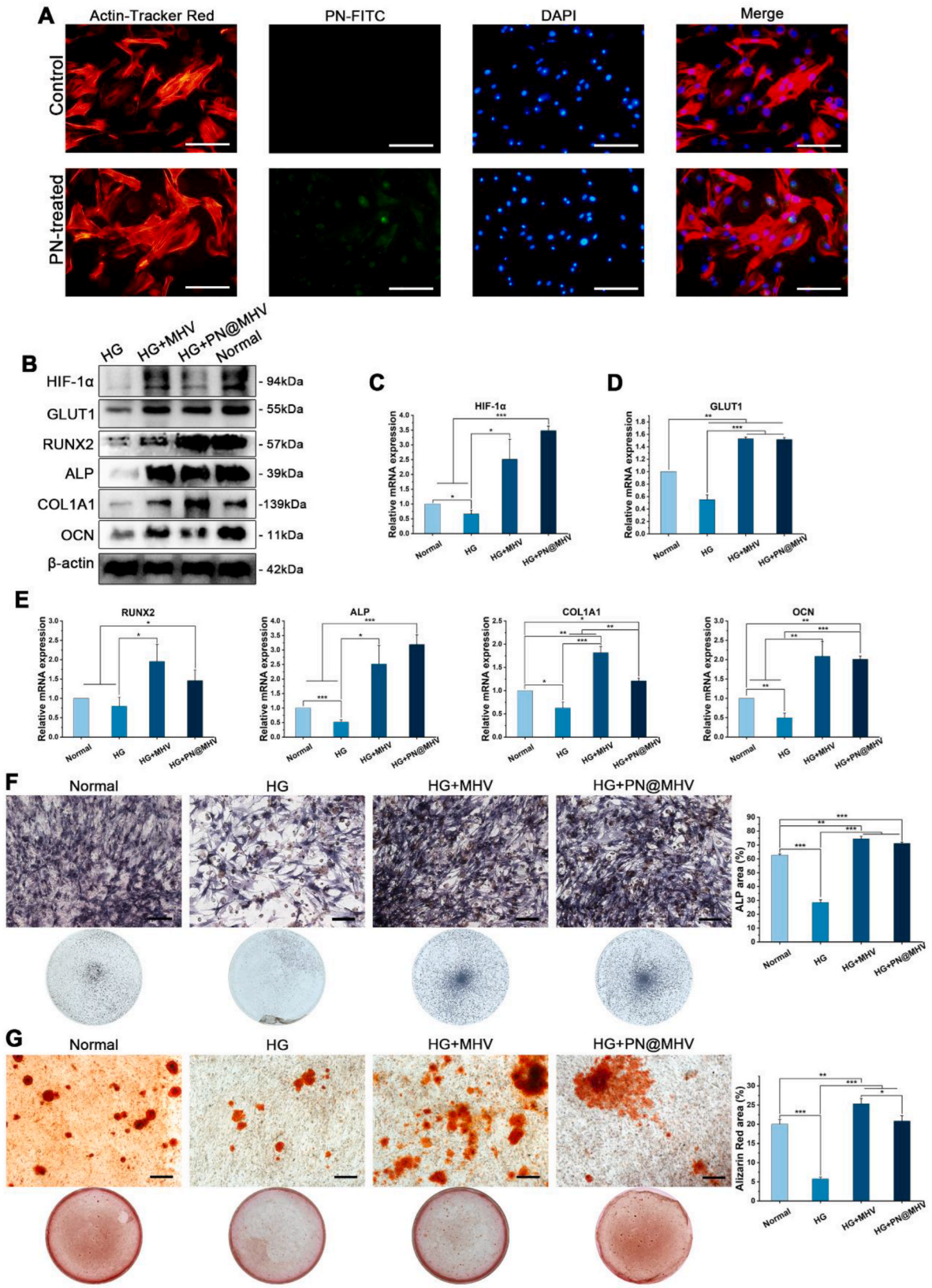

Fig. 8. PN@MHV hydrogel enhances osteoblast differentiation by promoting aerobic glycolysis under HG. (A) Fluorescence images of FITC-labelled nanoparticles and staining of DAPI and cytoskeleton in BMSCs. (B) Western blots of HIF-1α, GLUT1, RUNX2, ALP, COL1A1, OCN, and β-actin in BMSCs after 72 h of treatment. (C–E) Expression of HIF-1α, GLUT1, RUNX2, ALP, COL1A1, and OCN genes in BMSCs detected by RT-PCR after 48 h of treatment. (F) ALP staining of BMSCs and quantitative analysis after osteogenic induction for 7 days. (G) Alizarin Red staining of BMSCs and quantitative analysis of mineralized nodules accumulation after osteogenic induction for 21 days. Scale bar = 100 μm. All quantitative data are represented as mean ± SD (n = 3, *p < 0.05, **p < 0.01, ***p < 0.001).

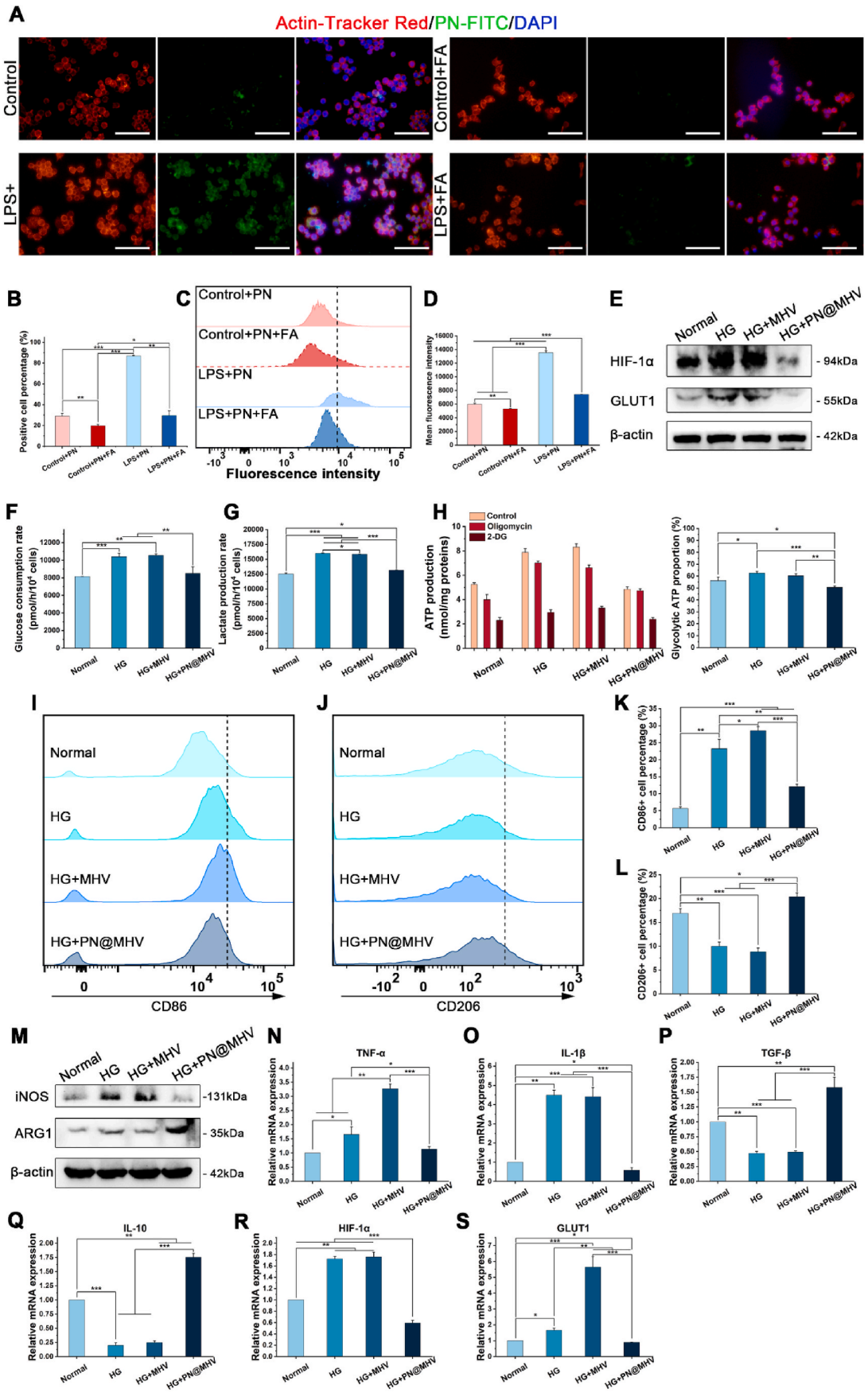

(caption on next page)

Fig. 9. PN@MHV hydrogel suppresses proinflammatory function by targeting M1 macrophages inhibiting aerobic glycolysis under HG. (A, B) Fluorescence images and quantitative analysis of FITC-labelled nanoparticles and staining of DAPI and cytoskeleton in RAW264.7. (C, D) Flow cytometry analysis of RAW264.7 uptake of FITC-labelled nanoparticles and quantitative analysis of mean fluorescence intensity. (E) Western blots of HIF-1α, GLUT1, and β-actin in RAW264.7 after 72 h of treatment. (F, G) Glucose consumption rate and lactate production rate in RAW264.7 after 48 h of treatment. (H) Levels of ATP in RAW264.7 after 24 h of treatment, and the proportion of glycolytic ATP to total ATP. (I, K) Flow cytometry analysis of CD86 expression in RAW264.7 and percentage of $CD86^+$ cells after 72 h of treatment. (J, L) Flow cytometry analysis of CD206 expression in RAW264.7 and percentage of $CD206^+$ cells after 72 h of treatment. (M) Western blots of iNOS, ARG1, and β-actin in RAW264.7 after 72 h of treatment. (N–S) Expression of TNF-α, IL-1β, TGF-β, IL-10, HIF-1α, and GLUT1 genes in RAW264.7 detected by RT-PCR after 48 h of treatment. Scale bar = 100 μm. All quantitative data are represented as mean ± SD (n = 3, *p < 0.05, **p < 0.01, ***p < 0.001).

was observed with MHV hydrogel treatment, while PN@MHV hydrogel treatment significantly reduced expression (Fig. 9E, R, S, S5). To further investigate the changes in cellular glycolysis, we examined the rate of glucose consumption, the rate of lactate production, and ATP production in macrophages. Showing synchronous changes with HIF-1α and GLUT1, the rates of glucose consumption and lactate production of macrophages were significantly increased under HG and decreased with PN@MHV hydrogel intervention (Fig. 9F and G). The proportion of ATP supply from glycolysis was increased under HG and could be significantly reduced with PN@MHV hydrogel intervention (Fig. 9H). Therefore, macrophage glycolysis was enhanced under HG, and PN@MHV hydrogel could suppress it, which was achieved by PN loaded in the hydrogel.

HG can drive macrophage proinflammatory gene expression and polarization towards the M1 phenotype, hence we subsequently examined the effect of hydrogels on macrophage polarization [39]. Flow cytometry analysis showed a significant increase in the M1 marker CD86 and the percentage of $CD86^+$ cells under HG, which was reduced following PN@MHV hydrogel treatment. Conversely, the M2 marker CD206 and the percentage of $CD206^+$ cells were decreased under HG but increased with hydrogel treatment (Fig. 9I, J, K, L). Further analysis by western blots revealed that iNOS levels were elevated under HG and significantly reduced with PN@MHV hydrogel intervention, the expression of proinflammatory cytokines TNF-α and IL-1β showed similar patterns (Fig. 9M, N, O, S5). Additionally, HG-induced suppression of ARG1 was alleviated by PN@MHV hydrogel treatment, and the expression of anti-inflammatory cytokines TGF-β and IL-10 mirrored this trend (Fig. 9M, P, Q, S5). These results suggest that PN@MHV hydrogel can suppress macrophage proinflammatory polarization and promote anti-inflammatory polarization through inhibition of macrophage glycolysis under HG.

3.9. PN@MHV hydrogel promotes fracture healing and improves inflammatory microenvironment in T2D mice

To confirm the effect of hydrogel in vivo, we further tested the hydrogel in a T2D mouse fracture model. We examined the fracture recovery of mice on 7, 14, and 21 days by using X-rays (Fig. 10A). Clear fracture gaps were observed on day 7 after fracture. On day 14, callus formation was observed, which was much smaller in the T2D group than in the normal group, and the hydrogel intervention could promote callus formation in T2D mice. Obvious calluses were all observed on day 21 (Fig. 10A). To further investigate the callus formation, we performed micro-CT analysis (Fig. 10B and C), which showed that total tissue volume (TV) in the T2D group was lower on day 14, and no difference was observed on day 21. High-density bone volume (BV) and bone volume fraction (BV/TV) were significantly lower in the T2D group on days 14 and 21 compared with the normal group, which increased significantly after hydrogel intervention. In addition, BV/TV was higher in the PN@MHV hydrogel group than in the MHV hydrogel group. Histomorphometrical analysis showed less fracture callus formation on day 14 and less new bone formation on day 21 at the fracture site in the T2D group compared with the normal group (Fig. 10D and E). Increased fracture callus formation on day 14 and a large amount of new bone formation resulting in sealing of the fracture site on day 21 were observed in the MHV and PN@MHV hydrogel groups (Fig. 10D and E), suggesting a satisfactory degree of fracture healing. These results suggest that T2D mice exhibit impaired bone regeneration due to dysfunctional callus formation and delayed mineralization, and that PN@MHV hydrogel accelerates these processes.

We further investigated the effect of hydrogels on macrophage polarization during fracture healing. Immunofluorescence staining results showed that on day 14 the T2D group had higher levels of iNOS and lower levels of CD206 compared with the normal group, and the expression of iNOS was decreased and CD206 was increased in the PN@MHV hydrogel group (Fig. 11A, B, E, F). In addition, MHV hydrogel had no significant effect on the expression of CD206. Therefore, PN@MHV hydrogel could promote the shift of proinflammatory M1 macrophages to anti-inflammatory M2, thereby improving the local inflammatory microenvironment of T2D fracture. Immunohistochemistry staining of bone tissue on day 21 showed that the expression of RUNX2 and OCN was significantly lower in the T2D group compared with the normal group, and the expression was significantly higher after hydrogel intervention (Fig. 11C, D, G, H). Therefore, PN@MHV hydrogel could effectively promote osteoblast differentiation in T2D mice, thereby promoting fracture healing. These results demonstrate that PN@MHV hydrogel can effectively promote fracture healing and improve the local inflammatory microenvironment in T2D mice.

4. Discussion

In this study, we constructed a novel drug delivery system comprising MYT cross-linked with HA-PBA and PVA hydrogels, which were further loaded with targeted nanoparticles (PN). The PN@MHV hydrogel bidirectionally regulates aerobic glycolysis in both osteoblasts and macrophages through the modulation of HIF-1α, thereby reshaping the immune microenvironment in T2D and enhancing fracture healing.

As a significant source of cellular energy, glycolysis has been extensively studied as an important source of cellular energy and revealed to profoundly influence cellular differentiation [18,37,40,41]. Enhanced glycolysis promotes proinflammatory M1 macrophage polarization and osteoblast differentiation [19,21]. However, in patients with T2D, the inflammatory microenvironment characterized by proinflammatory M1 macrophage overactivation is detrimental to tissue regeneration on the one hand, while on the other hand osteoblast differentiation is impaired and accompanied by abnormal glycolysis levels [11,12,42]. In alignment with previous findings, our results indicated a marked reduction in BMSCs at the fracture sites of T2D mice, alongside decreased expression levels of HIF-1α and GLUT1. In contrast, the population of proinflammatory macrophages was significantly elevated, correlating with increased expression levels of HIF-1α and GLUT1 [43]. These observations suggested that glycolysis alterations manifest differently across various cell types within the T2D fracture microenvironment. Many therapeutic strategies have been developed to regulate the inflammatory environment, promote angiogenesis, and promote osteoblast differentiation via modulation of cellular aerobic glycolysis to promote fracture healing in T2D patients [12,44–46]. However, many of these approaches focus on unidirectional regulation of glycolysis within a single cell type, often overlooking the interplay of multiple cell types and their complex glycolysis alterations. The crosstalk between these distinct cellular populations is likely to influence their differentiation and functional capacities, ultimately impacting the overall efficacy of therapeutic interventions.

Our findings indicate that MYT significantly promotes HIF-1α-

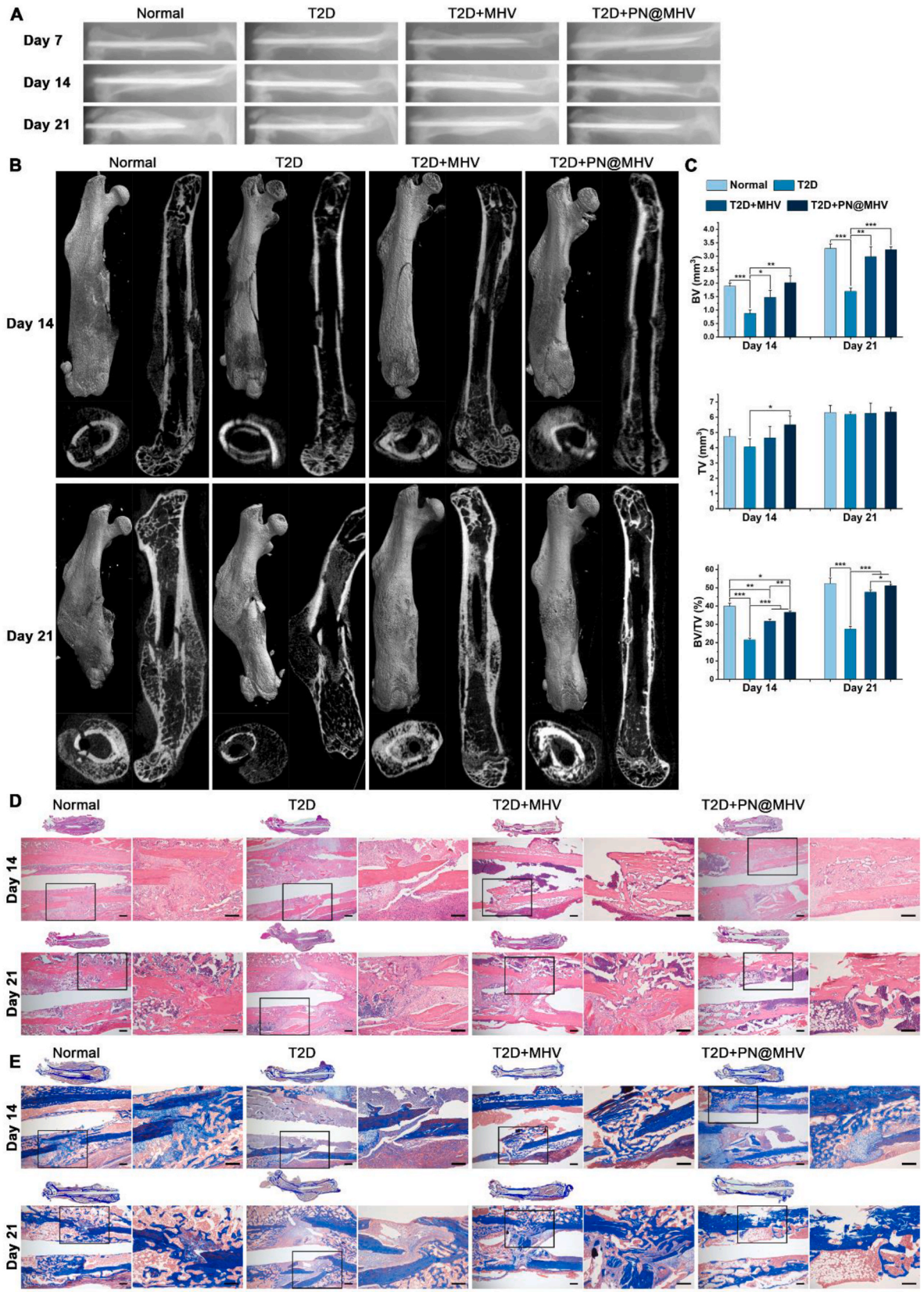

Fig. 10. PN@MHV hydrogel promotes T2D mice fracture healing. (A) Radiographic analysis of the fracture site on days 7, 14 and 21 after femur fracture. (B) 3D and 2D micro-CT images of the mouse femurs on days 14 and 21 after fracture. (C) Quantitative analysis of BV, TV, and BV/TV at the fracture site measured by micro-CT on days 14 and 21. (D) H&E staining of the femurs on days 14 and 21 after fracture. (E) Masson's trichrome staining of the femurs on days 14 and 21 after fracture. Scale bar = 100 μm. All quantitative data are represented as mean ± SD (n = 3 independent animals, *p < 0.05, **p < 0.01, ***p < 0.001).

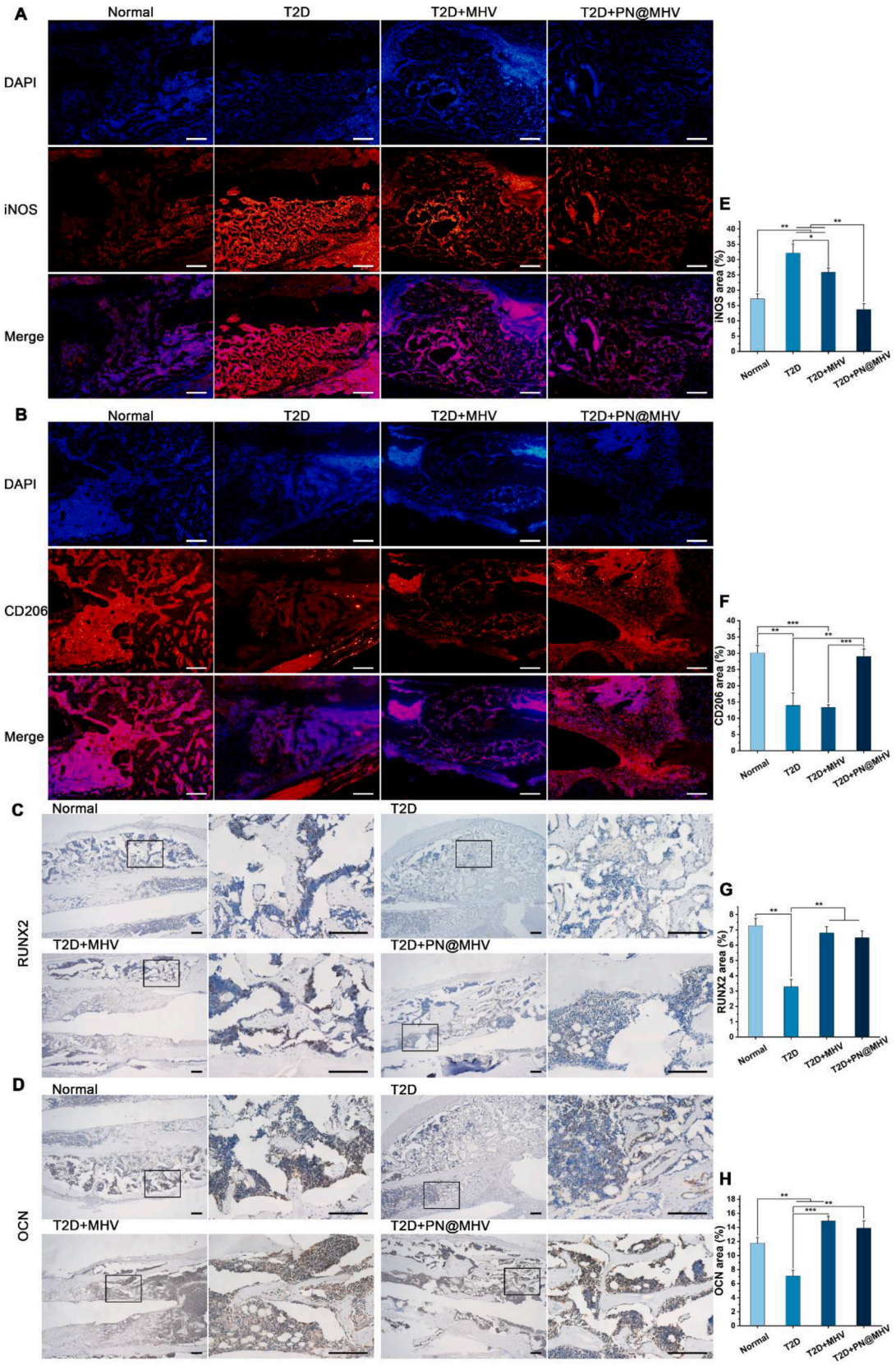

Fig. 11. PN@MHV hydrogel improves inflammatory microenvironment and enhances osteoblast differentiation in T2D mice. (A, E) Immunofluorescence staining and quantitative analysis of DAPI and iNOS at the fracture site on day 14 after femur fracture. (B, F) Immunofluorescence staining and quantitative analysis of DAPI and CD206 at the fracture site on day 14 after femur fracture. (C, G) Immunohistochemistry staining and quantitative analysis of RUNX2 at the fracture site on day 21 after femur fracture. (D, H) Immunohistochemistry staining and quantitative analysis of OCN at the fracture site on day 21 after femur fracture. Scale bar = 100 μm. All quantitative data are represented as mean ± SD (n = 3 independent animals, *p < 0.05, **p < 0.01, ***p < 0.001).

mediated glycolysis in BMSCs, corroborating previous studies that demonstrate the enhancement of glycolysis, which in turn facilitates osteoblast differentiation [20]. Interestingly, we hypothesized and confirmed that MYT can cross-link with HA-PBA and PVA to form a hydrogel, thus MYT can be slowly released with the degradation of the MHV hydrogel. The MHV hydrogel showed superior ability to promote osteoblast differentiation both in vivo and in vitro. Because of the excellent drug-loading function of the hydrogel, we incorporated PN into the MHV hydrogel to targeted inhibit the cellular HIF-1α-mediated glycolysis in response to the massive M1 polarization of macrophages in the T2D fracture microenvironment. We validated the ability of PN to target macrophages, and consistent with previous studies, the PN-loaded hydrogel successfully inhibited macrophage glycolysis to suppress the proinflammatory function promoting a shift to anti-inflammatory M2 phenotype. Moreover, it was demonstrated that the non-specific uptake of PN by BMSCs had no significant effect on glycolysis, and the PN@MHV hydrogel had excellent ability to facilitate osteoblast differentiation. Therefore, PN@MHV hydrogel successfully achieved bidirectional regulation of glycolysis in BMSCs and macrophages in response to the different changes in cellular glycolysis in the T2D fracture microenvironment. Consistent with previous studies, our study successfully promoted osteoblast differentiation and suppressed macrophage inflammation and consequently enhanced fracture healing by intervening against the glycolytic demands of cellular differentiation and function [12,23,24].

Fracture healing is a complex process involving multiple cells. In this study, we provide an idea for the treatment of fracture healing by considering the functions of multiple important cells in the bone microenvironment and regulating them individually, and the therapeutic strategy of multicellular targeting is also worthy of further research and development. The limitation of this study is that only the role of BMSCs and macrophages in the process of bone regeneration were considered. While MYT promotes the osteoblast differentiation of BMSC, it may also promote angiogenesis and thus enhance bone regeneration by up-regulating HIF-1α. The exploration of variations in cellular glycolysis under pathological circumstances provides a reliable entry point for the investigation of therapeutic mechanisms for clinical drugs. Changes in the function and state of different cells also provide a variety of possible targets for treatment and research.

Immune cell reprogramming, particularly macrophage polarization, is central to bone regeneration [8]. During the inflammatory phase of fracture repair and bone regeneration, M1 macrophages initiate essential processes by clearing necrotic tissue, recruiting BMSCs, and initiating osteogenic and angiogenic repair [47]. Transitioning to the reparative phase, M2 macrophages promote BMSC osteoblast differentiation through secretion of cytokines such as TGF-β, and extracellular vesicles [48]. Various hydrogels have been developed for strategies to achieve immunomodulation by engineering physicochemical properties (such as surface properties, conductivity, and pore size) and incorporating cytokines, extracellular vesicles, or anti-inflammatory molecules [11,49]. We here achieve immunomodulation by delivering drugs that intervene in the glycolytic pathway of cells. Because of the interaction between macrophages and BMSCs, this will be the focus of our future research.

HIF-1α expression is critical for stem cell homeostasis and deployment after injury [50]. Activation of HIF-1 responds to ROS production under hypoxia conditions and inhibits mitochondrial respiration to reduce ROS, preventing cellular damage caused by ROS accumulation [51]. Therefore, overproduction of ROS in BMSCs from diabetic patients may be due to the low expression levels of HIF-1α affecting HIF-1 activation and consequently impair the survival of BMSCs and the recruitment of BMSCs after fracture. The abnormality of hypoxic accumulation of HIF-1α in BMSCs in diabetes mellitus deserves further investigation. MYT's promotion of HIF-1α expression in BMSCs promotes cellular glycolysis for osteoblast differentiation on the one hand, and protects cells from ROS damage on the other.

5. Conclusion

In summary, we developed a hydrogel consisting of the drug MYT cross-linked with HA-PBA and PVA, incorporating PN. This hydrogel bidirectionally regulates HIF-1α-mediated glycolysis in both BMSCs and macrophages, thereby enhancing osteoblast differentiation while simultaneously suppressing inflammation through the controlled release of MYT and PN. The hydrogel's anti-inflammatory properties and its efficacy in promoting fracture healing were demonstrated in a T2D fracture mouse model.

CRediT authorship contribution statement

Shengming Zhang: Writing – original draft, Project administration, Formal analysis. **Weixian Hu:** Project administration, Methodology, Conceptualization. **Yanzhi Zhao:** Software, Project administration, Investigation. **Yuheng Liao:** Project administration, Investigation, Data curation. **Kangkang Zha:** Investigation, Formal analysis, Data curation. **Wenqian Zhang:** Validation, Resources, Methodology. **Chenyan Yu:** Project administration, Investigation, Formal analysis. **Jiewen Liao:** Methodology, Formal analysis, Data curation. **Hui Li:** Methodology, Funding acquisition. **Wu Zhou:** Software, Resources, Project administration, Funding acquisition. **Faqi Cao:** Methodology, Investigation, Funding acquisition, Formal analysis. **Bobin Mi:** Writing – review & editing, Writing – original draft, Supervision, Funding acquisition, Conceptualization. **Guohui Liu:** Writing – review & editing, Supervision, Funding acquisition, Conceptualization.

Ethics approval and consent to participate

All experiments were performed in accordance with the guidelines of the Animal Care and Use Committee at Tongji Medical College, Huazhong University of Science and Technology ([2023] IACUC Number: 4047).

Declaration of competing interest

The authors declare no conflict of interest.

Acknowledgements

This work was supported by the National Key R&D Program of China (2021YFA1101500), the National Science Foundation of China (82372406), the Fundamental Research Funds for the Central Universities (No. YCJJ20242417), Grants from Hubei Province Unveiling Science and Technology Projects (No. 2023AFB1096).

Appendix A. Supplementary data

Supplementary data to this article can be found online at https://doi.org/10.1016/j.bioactmat.2025.03.020.

References

[1] Q.M. Gao, Y.Y. Jiang, D.Y. Zhou, G.F. Li, Y.F. Han, J.Z. Yang, et al., Advanced glycation end products mediate biomineralization disorder in diabetic bone disease, Cell Reports Med. 5 (2024).
[2] L.C. Hofbauer, B. Busse, R. Eastell, S. Ferrari, M. Frost, R. Müller, et al., Bone fragility in diabetes: novel concepts and clinical implications, Lancet Diabetes Endocrinol. 10 (2022) 207–220.
[3] H.L. Jiao, E. Xiao, D.T. Graves, Diabetes and its effect on bone and fracture healing, Curr. Osteoporos. Rep. 13 (2015) 327–335.
[4] E. Standl, K. Khunti, T.B. Hansen, O. Schnell, The global epidemics of diabetes in the 21st century: current situation and perspectives, European J. Preventive Cardiology 26 (2019) 7–14.
[5] G.F. Xu, B.Y. Liu, Y.B. Sun, Y. Du, L.G. Snetselaar, F.B. Hu, et al., Prevalence of diagnosed type 1 and type 2 diabetes among US adults in 2016 and 2017: population based study, BMJ Br. Med. J. (Clin. Res. Ed.) 362 (2018).

[6] Y. Hu, Y. Xiong, R. Tao, H. Xue, L. Chen, Z. Lin, et al., Advances and perspective on animal models and hydrogel biomaterials for diabetic wound healing, Biomater. transl. 3 (2022) 188–200.
[7] Q. Zhang, W.K. Chen, G.F. Li, Z.X. Ma, M.R. Zhu, Q.M. Gao, et al., A factor-free hydrogel with ROS scavenging and responsive degradation for enhanced diabetic bone healing, Small 20 (2024).
[8] G.N. Duda, S. Geissler, S. Checa, S. Tsitsilonis, A. Petersen, K. Schmidt-Bleek, The decisive early phase of bone regeneration, Nat. Rev. Rheumatol. 19 (2023) 78–95.
[9] L. Claes, S. Recknagel, A. Ignatius, Fracture healing under healthy and inflammatory conditions, Nat. Rev. Rheumatol. 8 (2012) 133–143.
[10] M.Y. Donath, S.E. Shoelson, Type 2 diabetes as an inflammatory disease, Nat. Rev. Immunol. 11 (2011) 98–107.
[11] Y.L. Wang, Q.S. Lin, H. Zhang, S.C. Wang, J. Cui, Y. Hu, et al., M2 macrophage-derived exosomes promote diabetic fracture healing by acting as an immunomodulator, Bioact. Mater. 28 (2023) 273–283.
[12] F.F. Song, W.D. Lee, T. Marmo, X. Ji, C. Song, X.Y. Liao, et al., Osteoblast-intrinsic defect in glucose metabolism impairs bone formation in type II diabetic male mice, Elife 12 (2023).
[13] J. Verhaeghe, E. van Herck, W.J. Visser, A.M. Suiker, M. Thomasset, T.A. Einhorn, et al., Bone and mineral metabolism in BB rats with long-term diabetes. Decreased bone turnover and osteoporosis, Diabetes 39 (1990) 477–482.
[14] E.J. Lee, M.K. Kang, Y.H. Kim, D.Y. Kim, H. Oh, S.I. Kim, et al., Coumarin ameliorates impaired bone turnover by inhibiting the formation of advanced glycation end products in diabetic osteoblasts and osteoclasts, Biomolecules 10 (2020).
[15] S.J. Kierans, C.T. Taylor, Regulation of glycolysis by the hypoxia-inducible factor (HIF): implications for cellular physiology, J. Physiol.-London 599 (2021) 23–37.
[16] O. Warburg, On the origin of cancer cells, Science (New York, NY) 123 (1956) 309–314.
[17] M.G.V. Heiden, L.C. Cantley, C.B. Thompson, Understanding the warburg effect: the metabolic requirements of cell proliferation, Science 324 (2009) 1029–1033.
[18] S.C. Cheng, J. Quintin, R.A. Cramer, K.M. Shepardson, S. Saeed, V. Kumar, et al., mTOR- and HIF-1α-mediated aerobic glycolysis as metabolic basis for trained immunity, Science 345 (2014) 1579. -+.
[19] E. Esen, J.Q. Chen, C.M. Karner, A.L. Okunade, B.W. Patterson, F.X. Long, WNT-LRP5 signaling induces warburg effect through mTORC2 activation during osteoblast differentiation, Cell Metab. 17 (2013) 745–755.
[20] W.C. Lee, X. Ji, I. Nissim, F.X. Long, Malic enzyme couples mitochondria with aerobic glycolysis in osteoblasts, Cell Rep. 32 (2020).
[21] G.M. Tannahill, A.M. Curtis, J. Adamik, E.M. Palsson-McDermott, A.F. McGettrick, G. Goel, et al., Succinate is an inflammatory signal that induces IL-1β through HIF-1α, Nature 496 (2013) 238. -+.
[22] E.L. Mills, B. Kelly, A. Logan, A.S.H. Costa, M. Varma, C.E. Bryant, et al., Succinate dehydrogenase supports metabolic repurposing of mitochondria to drive inflammatory macrophages, Cell 167 (2016) 457. -+.
[23] S.T. Liao, C. Han, D.Q. Xu, X.W. Fu, J.S. Wang, L.Y. Kong, 4-Octyl itaconate inhibits aerobic glycolysis by targeting GAPDH to exert anti-inflammatory effects, Nat. Commun. 10 (2019).
[24] W.K.E. Ip, N. Hoshi, D.S. Shouval, S. Snapper, R. Medzhitov, Anti-inflammatory effect of IL-10 mediated by metabolic reprogramming of macrophages, Science 356 (2017) 513–519.
[25] J. Yang, S.S. Li, Z.Y. Li, L.T. Yao, M.J. Liu, K.L. Tong, et al., Targeting YAP1-regulated glycolysis in fibroblast-like synoviocytes impairs macrophage infiltration to ameliorate diabetic osteoarthritis progression, Adv. Sci. 11 (2024).
[26] G.L. Semenza, Hypoxia-inducible factors in physiology and medicine, Cell 148 (2012) 399–408.
[27] W.Q. Zhang, K.K. Zha, Y. Xiong, W.X. Hu, L. Chen, Z. Lin, et al., Glucose-responsive, antioxidative HA-PBA-FA/EN106 hydrogel enhanced diabetic wound healing through modulation of FEM1b-FNIP1 axis and promoting angiogenesis, Bioact. Mater. 30 (2023) 29–45.
[28] E. Ilegems, G. Bryzgalova, J. Correia, B. Yesildag, E. Berra, J.L. Ruas, et al., HIF-1α inhibitor PX-478 preserves pancreatic. cell function in diabetes, Sci. Transl. Med. 14 (2022).
[29] J.J. Zhong, X.J. Mao, H.Y.Z. Li, G.R. Shen, X. Cao, N. He, et al., Single-cell RNA sequencing analysis reveals the relationship of bone marrow and osteopenia in STZ-induced type 1 diabetic mice, J. Adv. Res. 41 (2022) 145–158.
[30] W. Wagner, A.D. Ho, Mesenchymal stem cell preparations - comparing apples and oranges, Stem Cell Rev. 3 (2007) 239–248.
[31] J.W. Wei, J. Shimazu, M.P. Makinistoglu, A. Maurizi, D. Kajimura, H.H. Zong, et al., Glucose uptake and Runx2 synergize to orchestrate osteoblast differentiation and bone formation, Cell 161 (2015) 1576–1591.
[32] C.J. Hu, S. Iyer, A. Sataur, K.L. Covello, L.A. Chodosh, M.C. Simon, Differential regulation of the transcriptional activities of hypoxia-inducible factor 1 alpha (HIF-1α) and HIF-2α in stem cells, Mol. Cell Biol. 26 (2006) 3514–3526.
[33] P. Aguiari, S. Leo, B. Zavan, V. Vindigni, A. Rimessi, K. Bianchi, et al., High glucose induces adipogenic differentiation of muscle-derived stem cells, Proc. Natl. Acad. Sci. U. S. A. 105 (2008) 1226–1231.
[34] T.Z. Yu, J.L. Robotham, Y. Yoon, Increased production of reactive oxygen species in hyperglycemic conditions requires dynamic change of mitochondrial morphology, Proc. Natl. Acad. Sci. U. S. A. 103 (2006) 2653–2658.
[35] P. Zhang, J. Liao, X.J. Wang, Z.P. Feng, High glucose promotes apoptosis and autophagy of MC3T3-E1 osteoblasts, Arch. Med. Sci. 19 (2023) 138–150.
[36] A. Rezaei, Y.T. Li, M. Turmaine, S. Bertazzo, C.A. Howard, T.R. Arnett, et al., Hypoxia mimetics restore bone biomineralisation in hyperglycaemic environments, Sci. Rep. 12 (2022).
[37] D. Zhang, Z.Y. Tang, H. Huang, G.L. Zhou, C. Cui, Y.J. Weng, et al., Metabolic regulation of gene expression by histone lactylation, Nature 574 (2019) 575. -+.
[38] W. Xia, A.R. Hilgenbrink, E.L. Matteson, M.B. Lockwood, J.X. Cheng, P.S. Low, A functional folate receptor is induced during macrophage activation and can be used to target drugs to activated macrophages, Blood 113 (2009) 438–446.
[39] L. Edgar, N. Akbar, A.T. Braithwaite, T. Krausgruber, H. Gallart-Ayala, J. Bailey, et al., Hyperglycemia induces trained immunity in macrophages and their precursors and promotes atherosclerosis, Circulation 144 (2021) 961–982.
[40] M. Peng, N. Yin, S. Chhangawala, K. Xu, C.S. Leslie, M.O. Li, Aerobic glycolysis promotes T helper 1 cell differentiation through an epigenetic mechanism, Science 354 (2016) 481–484.
[41] A. Moussaieff, M. Rouleau, D. Kitsberg, M. Cohen, G. Levy, D. Barasch, et al., Glycolysis-mediated changes in acetyl-CoA and histone acetylation control the early differentiation of embryonic stem cells, Cell Metab. 21 (2015) 392–402.
[42] A.S. Kimball, F.M. Davis, A. DenDekker, A.D. Joshi, M.A. Schaller, J. Bermick, et al., The histone methyltransferase Setdb2 modulates macrophage phenotype and uric acid production in diabetic wound repair, Immunity 51 (2019) 258. -+.
[43] W.R. Francis, Z. Liu, S.E. Owens, X. Wang, H. Xue, A. Lord, et al., Role of hypoxia inducible factor 1 alpha in cobalt nanoparticle induced cytotoxicity of human THP-1 macrophages, Biomater. transl. 2 (2021) 143–150.
[44] C.J. You, F.Y. Shen, P.Y. Yang, J.Y. Cui, Q.Y. Ren, M.Y. Liu, et al., O-GlcNAcylation mediates Wnt-stimulated bone formation by rewiring aerobic glycolysis, EMBO Rep. (2024).
[45] H.R. Du, B. Li, R. Yu, X.X. Lu, C.L. Li, H.H. Zhang, et al., ETV2 regulating PHD2-HIF-1α axis controls metabolism reprogramming promotes vascularized bone regeneration, Bioact. Mater. 37 (2024) 222–238.
[46] J.L. Jin, Y.Q. Yang, J. Yang, Z.Y. Sun, D.Y. Wang, Y.F. Qin, et al., Macrophage metabolic reprogramming-based diabetic infected bone defect/bone reconstruction though multi-function silk hydrogel with exosome release, Int. J. Biol. Macromol. 278 (2024).
[47] L.J. Raggatt, M.E. Wullschleger, K.A. Alexander, A.C.K. Wu, S.M. Millard, S. Kaur, et al., Fracture healing via periosteal callus formation requires macrophages for both initiation and progression of early endochondral ossification, Am. J. Pathol. 184 (2014) 3192–3204.
[48] Y.H. Wang, C.Z. Zhao, R.Y. Wang, Q.X. Du, J.Y. Liu, J. Pan, The crosstalk between macrophages and bone marrow mesenchymal stem cells in bone healing, Stem Cell Res. Ther. 13 (2022).
[49] M. Fu, C.S. Yang, G.X. Sun, Recent advances in immunomodulatory hydrogels biomaterials for bone tissue regeneration, Mol. Immunol. 163 (2023) 48–62.
[50] M. Schieber, N.S. Chandel, ROS function in redox signaling and oxidative stress, Curr. Biol. 24 (2014) R453–R462.
[51] J.W. Kim, I. Tchernyshyov, G.L. Semenza, C.V. Dang, HIF-1-mediated expression of pyruvate dehydrogenase kinase: a metabolic switch required for cellular adaptation to hypoxia, Cell Metab. 3 (2006) 177–185.